Check for updates

*Advanced Materials*

ADVANCED MATERIALS
www.advmat.de

RESEARCH ARTICLE OPEN ACCESS

# Microgels Enable iPSCs to Assemble, Expand, and Differentiate Into Organoids—From Sizable to High-Throughput

Laura Klasen[1,2] | Matthias Mork[1,2] | Ramin Nasehi[1,2] | Vasudha Turuvekere Krishnamurthy[2,3] | Kira Zeevaert[4,5] | Aaron Babendreyer[6] | Jacopo Di Russo[2,3] | Wolfgang Wagner[4,5] | Laura De Laporte[1,2,7]

[1]Institute For Technical and Macromolecular Chemistry, RWTH Aachen University, Aachen, Germany | [2]DWI—Leibniz Institute for Interactive Materials e.V., Aachen, Germany | [3]Institute of Molecular and Cellular Anatomy, RWTH Aachen University, Aachen, Germany | [4]Helmholtz-Institute For Biomedical Engineering, RWTH Aachen University, Aachen, Germany | [5]Institute For Stem Cell Biology, RWTH Aachen University Medical School, Aachen, Germany | [6]Institute of Molecular Pharmacology, University Hospital RWTH Aachen University, Aachen, Germany | [7]Department of Advanced Materials For Biomedicine (AMB), CBMS—Center For Biohybrid Medical Systems, AME—Institute of Applied Medical Engineering, University Hospital RWTH Aachen, Aachen, Germany

**Correspondence:** Laura De Laporte (delaporte@dwi.rwth-aachen.de)

**Received:** 30 March 2026 | **Revised:** 20 July 2026 | **Accepted:** 15 September 2026

**Keywords:** cellular differentiation | drug development | germ layer | induced pluripotent stem cell | microfluidics | nanotechnology | organoid | peg ratio | personalized medicine

## ABSTRACT

Organoid research holds tremendous potential for personalized medicine and drug development. However, current limitations include reproducibility issues largely due to the use of biologically derived materials, which are prone to batch-to-batch variations. Here, we report a chemically defined microgel-based method for human induced pluripotent stem cell (iPSC)-based organoid generation, enabling expansion of iPSCs and their subsequent differentiation within one construct across different scales, including compatibility with automated 384-well plate workflows. Chemically defined poly(ethylene glycol) (PEG)-based microgels are produced via parallelized step-emulsification microfluidics, enabling scalable production. This approach leverages the self-organization of iPSCs with microgels to build three-dimensional constructs, driven by robust cell-material interactions achieved through vitronectin-coated PEG microgels. This technology allows the iPSCs to expand and retain their pluripotency, after which they can be differentiated into the three germ layers, providing a suitable platform for organoid differentiation. This was further extended by differentiation into cardiac organoids and retinal photoreceptors to demonstrate two exemplary tissues.

## 1 | Introduction

Organoids are three-dimensional in vitro organ model systems of increasing interest in biomedical research for disease modeling and next-generation drug screening and development [1]. Due to their derivation from either pluripotent stem cells or organ-specific progenitor cells, organoids are developed for an increasing number of organs, including the liver [2–4], heart [5–7], brain [8–10], and retina [11, 12]. Induced pluripotent stem cells (iPSCs) are somatic cells reprogrammed to a pluripotent state through the forced expression of specific transcription factors, enabling self-renewal and differentiation into all germ layers. They provide a more ethically sustainable and accessible alternative to embryonic stem cells (ESCs) [13]. They have great potential in personalized medicine and organoid research and are receiving increasing attention [14].

Laura Klasen and Matthias Mork contributed equally to this work.

This is an open access article under the terms of the Creative Commons Attribution License, which permits use, distribution and reproduction in any medium, provided the original work is properly cited.
© 2026 The Author(s). *Advanced Materials* published by Wiley-VCH GmbH

In addition to advances in cell types, organoid research has also progressed by introducing various biomaterials that form scaffolds to enhance the cellular organization, stability, and uniformity [15], and the functionality of the resulting organoids [16–18]. Hydrogels that mimic the extracellular matrix (ECM), e.g., Matrigel [19], collagen [20, 21], fibrin [22, 23], hyaluronic acid (HA) [24], or decellularized tissue [25–27] are the main biomaterials used in organoid research. Since these biologically derived materials persistently demonstrate high batch-to-batch variability and could have tumorigenic potential [19, 28], the necessity arises for chemically well-defined biomaterial systems for organoid research [28–30], with one of the most frequently utilized synthetic hydrogels being poly(ethylene glycol) (PEG) [31, 32].

One main challenge in 3D tissue models is to grow dense functional tissue due to the reduced proliferation of many mature cells and insufficient diffusion. On the other hand, iPSCs have a high expansion potential but start to differentiate in an uncontrolled manner inside 3D hydrogels due to the many signals provided by the materials that highly influence cellular processes [33]. Therefore, a 3D hydrogel system that allows for iPSC expansion into dense cellular constructs and sequential controlled differentiation in the same construct can bridge this gap. Previous work has demonstrated that maintaining the self-renewal hallmark of the stem cell phenotype and, thereby, the proliferation capacity, in 3D hydrogels can be promoted by enhancing cell-cell interaction by the use of very dynamic [34] or fast degradable [35] hydrogels or the addition of single-cell survival-enhancing supplements [36].

In recent years, microporous annealed particle (MAP) scaffolds have emerged to enhance cell growth and infiltration by providing more empty space. MAP scaffolds are 3D constructs assembled by microgels and exhibit pore interconnectivity with micron-scale pores compared to conventional nanoporous hydrogels that must be degraded to provide sufficient space for the cells. Therefore, MAP scaffolds offer an alternative to bulk hydrogels that rely on an intricate balance between degradability and mechanical support to enable tissue formation [37–41]. MAP scaffolds pose great potential for stem cell-based research, demonstrated by their use with mesenchymal stem cells (MSCs) [42, 43]. To produce monodisperse spherical microdroplets and -gels at high production rates, parallelized microfluidic step-emulsification has emerged as a suitable method compared to single-channel microfluidic systems [44, 45].

Here, we demonstrate that iPSC-induced assembly of microgels resulted in millimeter-scale or high-throughput scaffolds that support iPSC growth while maintaining their stemness, allowing for sequential controlled differentiation at defined time points. PEG-based biomaterials, microgel scaffolds, adhesion proteins, and automated organoid workflows have individually advanced tissue engineering; however, their integration into a single chemically defined platform that supports iPSC expansion and subsequent differentiation has not been reported. Scalability of the microgel building block production is crucial for meeting the demands of growing larger organoids and high-throughput applications. We present a new method to grow human tissues in vitro in a reproducible and scalable manner by combining iPSC-based organoid technologies with microgel-based biomaterials in a chemically defined system. We hypothesized that this would be possible due to the high level of cell-cell interactions that this method allows for, in addition to facilitating diffusion through the microgel networks. Our scalable strategy is based on self-organized scaffolds built by iPSCs using functionalized PEG-based spherical microgels, yielding 3D constructs that allow for self-controlled expansion and guided differentiation. Microdroplets composed of PEG-diacrylate (PEG-DA) and glycidyl methacrylate (GMA) were fabricated by parallelized step-emulsification in a microfluidic device. Conversion into microgels is achieved by photoinitiated free-radical polymerization in-flow. The microgels were post-modified with vitronectin by amine-epoxy coupling to the epoxide moieties of the GMA incorporated into the polymer matrix. To demonstrate the large versatility and relevance of this system, sequential differentiation into the three germ layers is shown, and iPSC-derived cardiac organoids and retinal cells were generated. Additionally, we established the scalability and compatibility of our approach with an automated liquid handling system, supporting its potential future use in high-throughput production workflows for compound screening during drug development and disease modeling.

### 1.1 | Large-Scale Microfluidic Production and Biofunctionalization of Spherical PEG-Based Microgels

To generate sufficient quantities of functionalized spherical microgels for iPSC-induced 3D assembly, we developed a parallelized step-emulsification microfluidic device (Figure 1a). The dispersed phase, carrying the microgel precursors, is transferred through individual microchannels, and droplet formation is achieved by expansion into the deep oil reservoir. Through parallelization of these microchannels, we generated microdroplets with an average diameter of ~ 80 µm, achieving a production rate in the range of $10^7$ droplets per hour (Figure S1 and Video S1). After generation, the droplets were transferred off-chip through an outlet tube and photocrosslinked in the outlet tubing by UV irradiation in flow. We supplemented the microgel precursor solution with glycidyl methacrylate (GMA) to introduce epoxide moieties into the microgel network, enabling us to specifically bind vitronectin (VTN) or other amine-bearing molecules to the microgels. Vitronectin was used to support iPSC adhesion and maintenance of the pluripotent state [46]. The incorporation of GMA was qualitatively analyzed by confocal imaging after post-functionalization with fluoresceinamine-isomer I (Figure 1b). Here, specific binding was exclusively observed for GMA-modified microgels, revealing the successful incorporation of accessible epoxide functionalities into the microgel network.

Subsequently, we investigated the efficiency of VTN post-functionalization via qualitative confocal imaging after staining with a fluorescent VTN antibody (Figure 1d). Sufficient coverage of VTN on the microgel surface was exclusively indicated for GMA-modified microgels. To investigate the mechanical properties of the microgels, we performed nanoindentation in different buffered solutions (Figure 1e). Generally, stiffness was slightly lower in 1x PBS solution as compared to culture media, with no significant differences between GMA-modified microgels with or without VTN post-functionalization. For all tested conditions, the average stiffness ranges were below 50 kPa, which is within



15214095, 0, Downloaded from https://advanced.onlinelibrary.wiley.com/doi/10.1002/adma.75116, Wiley Online Library on [27/09/2026]. See the Terms and Conditions (https://onlinelibrary.wiley.com/terms-and-conditions) on Wiley Online Library for rules of use; OA articles are governed by the applicable Creative Commons License

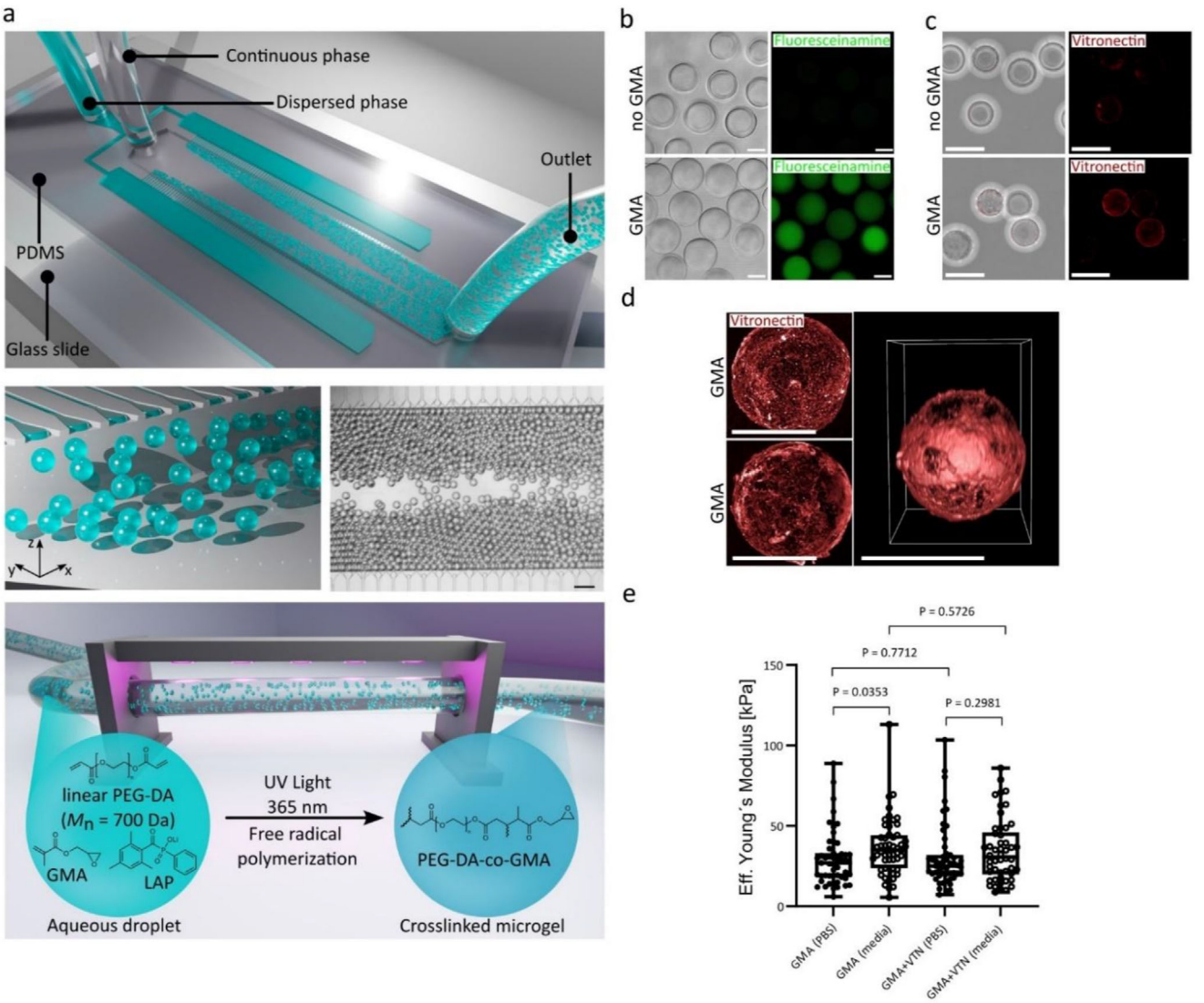



**FIGURE 1** | Large-scale production and functionalization of spherical microgels for iPSC-induced assembly. (a) Top: Schematic of a parallelized step-emulsification microfluidic device used to produce spherical aqueous droplets, composed of PEG-DA, co-monomer GMA, and photoinitiator Lithium-Phenyl-2,4,6-trimethylbenzoylphosphinat (LAP). Middle: Schematic of droplet generation achieved via expansion of the aqueous phase from the shallow microchannel into the deep oil reservoir with corresponding microscope image (scale bar: 200 μm). Bottom: Schematic of in-flow UV polymerization in the outlet tube, transforming the pre-polymer droplets into polymerized PEG-DA-co-GMA microgels. Schematics are prepared with Blender. (b) Confocal images of fluoresceinamine isomer I (green) labelled PEG microgels to demonstrate amine coupling to the GMA-modified microgels. Top: Pure PEG-DA microgels revealed no specific binding of fluoresceinamine isomer I due to the lack of epoxy moieties. Bottom: PEG-DA-co-GMA microgels show specific binding of fluoresceinamine isomer I to the free epoxy moieties. Scale bars represent 40 μm. (c) Confocal images of PEG microgels stained for VTN with fluorescent VTN-antibody. Top: PEG-DA microgels post-functionalized with VTN. Bottom: PEG-DA-co-GMA microgels post-functionalized with VTN. Scale bar represents 100 μm. (d) Magnified confocal images of VTN-functionalized PEG-DA-co-GMA microgels. Left: two distinct microgels exhibiting comparable VTN distribution on the surface. Right: 3D reconstruction visualizing the VTN distribution on a VTN functionalized PEG-DA-co-GMA microgel. Scale bars represent 50 μm. (e) Mechanical properties of GMA-modified and VTN post-functionalized microgels in different buffered solutions, determined via nanoindentation. Statistical analysis was performed via an unpaired *t*-test ($n = 50–55$).

the relevant stiffness range for specific tissues in vivo, like the myocardium [47].

## 1.2 | Microgels Enable mm-Scale Scaffolds for iPSC Expansion and Differentiation

Subsequently, biocompatibility and cell-material interaction with iPSCs were evaluated. The iPSCs only adhered well to the VTN-functionalized microgels, which could be observed in the three-dimensional cell-microgel clustering (Figure 2a, Figure S2). This demonstrated the necessity of both the GMA incorporation and the VTN functionalization, as microgel-cell cluster formation did not occur in conditions without the amine-epoxy-based biofunctionalization. Subsequently, we confirmed the preservation of pluripotency for the iPSCs cultured with the microgels for 4 days by staining for OCT4. Actin concentration around the microgels was observed (Figure 2b), further indicating the



15214095, 0, Downloaded from https://advanced.onlinelibrary.wiley.com/doi/10.1002/adma.75116, Wiley Online Library on [27/09/2026]. See the Terms and Conditions (https://onlinelibrary.wiley.com/terms-and-conditions) on Wiley Online Library for rules of use; OA articles are governed by the applicable Creative Commons License

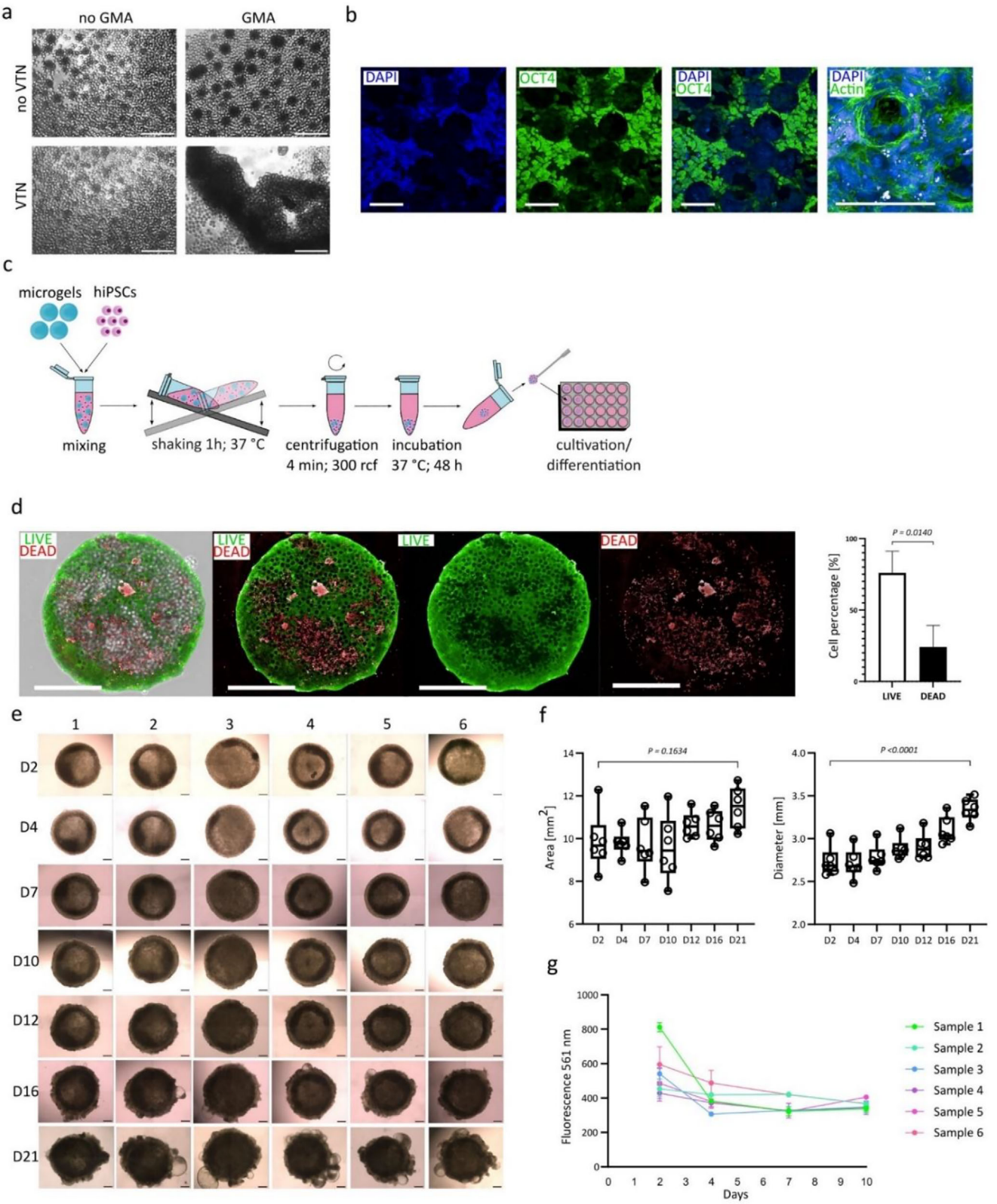



**FIGURE 2** | Production, viability, and reproducibility of 3D iPSC scaffolds. (a) VTN functionalization via amine-epoxy coupling (GMA) to enable cell attachment to the microgels (brightfield images on day 4; scale bar is 500 μm). The incorporation of GMA and the functionalization with VTN are both essential to achieve adequate cell-material interactions. (The images in larger sizes and higher magnification images of the experiment for better visualization can be found in Figure S2) (b) Cell-material interaction between PEG-based microgels and iPSCs. Images 1–3: Pluripotency verification (OCT4) of iPSCs on PEG-DA-co-GMA microgels (DAPI (blue), OCT4 (green); scale bar is 100 μm). Immunofluorescence staining was performed on day 4. Image 4: Cell-material interaction demonstrated by Actin filament clustering at the interface. (DAPI (blue), Actin (phalloidin, green), scale bar is 100 μm). (c) Schematic illustration of mm-scale scaffold production method (prepared with Inkscape) using iPSCs and PEG-microgels. (d) LIVE/DEAD



15214095, 0, Downloaded from https://advanced.onlinelibrary.wiley.com/doi/10.1002/adma.75116, Wiley Online Library on [27/09/2026]. See the Terms and Conditions (https://onlinelibrary.wiley.com/terms-and-conditions) on Wiley Online Library for rules of use; OA articles are governed by the applicable Creative Commons License

proper iPSC-material interaction. With the confirmation of iPSC-material compatibility and the ability of the iPSCs to maintain their stemness, we developed a protocol for the formation of mm-scale microgel-iPSC constructs (Figure 2c), subsequently referred to as scaffolds, which relies on the material-cell interaction to provide mechanical stability and integrity while allowing sufficient oxygen/nutrition diffusion.

We optimized the iPSC-microgel ratio to ~400 000 cells/4332 microgels (~92 cells/microgel) (Figure S3), enabling reproducible generation of size- and shape-consistent scaffolds. To ensure a replicable scaffold size, the number of microgels used in the experiments was determined from the used microgel suspension volume using a calibration curve generated by brightfield image-based quantification (Figure S4). These scaffolds were mechanically stable after 48 h and could be transferred and cultured in solution in 24-well plates for the remaining culture or differentiation time. After 48 h, we observed an average cell viability of 75.92% ± 15.21% (Figure 2d), describing a moderately reduced viability compared with conventional embryoid body formation, which often shows cell death of ~10% after 48 h and ~ 50% after 5 days [48]. The direct comparison, however, is limited since the microgel-iPSC scaffolds described here were generated with a substantially higher initial cell number of approximately 400 000 cells, resulting in larger constructs than the typical embryoid bodies reported in the literature. The increased scaffold size and culturing conditions during the first 48 h on the bottom of a conical tube could restrict nutrient and oxygen access. Therefore, the observed reduction in viability is most likely due to the initial starting cell number and culture geometry. The produced cell-biomaterial scaffolds had a mean area of 9.88 ± 1.35 $mm^2$ (cross-section) and a diameter of 2.73 ± 0.17 mm after 48 h of culture. Furthermore, we monitored the mechanical stability and reproducibility of the scaffolds, demonstrating uniform spherical constructs that could be cultured in suspension without deformation or breakage over the course of 21 days (Figure 2e). During this time, we observed continuous growth of the scaffolds up to an area of 11.47 ± 0.97 $mm^2$ and a diameter of 3.34 ± 0.13 mm, demonstrating the iPSC expansion capability of the system (Figure 2f). The area measurements hereby demonstrated a higher variability because the scaffolds were not perfectly circular, making the two-dimensional area more sensitive to irregular construct morphologies than the single-axis diameter measurements. The metabolic activity was measured by the fluorescence shift caused through the enzymatic reduction of resazurin to resorufin by metabolically active cells and supported the reproducibility between multiple scaffolds. A high metabolic activity was measured after 48 h, which balanced out to a stable level after 4 days (Figure 2g). Microgels provide stability and introduce highly diffusible regions into the otherwise dense cellular constructs, through which oxygen, nutrient, and waste transport could be improved [49]. This may facilitate mass transport within the microgel-iPSC scaffolds, thereby offering a potential novel platform for the development of mm-scale organoids. Diffusion of oxygen through the cell/microgel constructs was numerically simulated, suggesting that the presence of microgels may increase oxygen availability within the scaffold.

### 1.3 | Directed Differentiation of Microgel-iPSC Scaffolds

We analyzed whether iPSCs maintained differentiation potential in the scaffolds by inducing differentiation toward the three germ layers. After 48 h of expansion, we used directed differentiation protocols and analyzed the scaffolds after 7 days of differentiation at the protein, gene expression, and epigenetic levels. Immunostaining for germ layer-specific markers (endoderm: GATA4; ectoderm: PAX6; mesoderm: Brachyury) showed expression of the respective markers upon directed differentiation (Figure 3a). We further applied the PluripotencyScreen technology [50], which is based on a combination of site-specific DNA methylation (DNAm) assays to characterize iPSCs and their differentiation potential (Figures 3b,c and S5). A pluripotency score is indicative of pluripotency, whereas differentiation scores for mesoderm, endoderm, and ectoderm are indicative of early cell-fate decisions toward respective lineages (Figure 3b). Deconvolution against a reference matrix provides further estimates of the cellular composition (Figure 3c). In the nondifferentiated scaffolds, the iPSCs maintained a relatively high pluripotency score, albeit some DNA methylation changes point toward endodermal differentiation. This could be due to the high surface area presented by the microgels. Furthermore, three lineage differentiations evoked epigenetic modifications indicative of differentiation toward mesoderm, ectoderm, and endoderm, respectively (Figure 3b). These findings were further supported by gene expression analysis of marker genes based on RT–qPCR (Figure 3d,e). We thereby demonstrated the potential of iPSCs to assemble microgels into mm-sized constructs with the ability to expand until controlled differentiation is induced.

Subsequently, we evaluated whether this technology can be used for cardiac organoid formation, as this reflects functionality and cell interconnectivity by spontaneous beating characteristics. After 48 h of expansion within the microgel construct, the cardiac differentiation protocol was initiated. The scaffolds exhibited mechanical stability and shape consistency during 23 days of cardiac differentiation (Figure 4a). We further observed the reproducibility of shape and size of these organoids during the differentiation process, as well as the expression of the cardiomyocyte marker cardiac troponin T (cTnT) (Figure 4b). The distribution of cTnT across the cardiac organoid demonstrated

assay of scaffold after 2 days of culture (live cells (green), dead cells (red)). Right: confocal Z-stack images (680 µm, Scale bar: 1 mm); left: cell viability analysis of LIVE/DEAD assay images using ImageJ ($n = 3$, statistical significance was calculated via unpaired $t$-test). (e, f) Reproducibility and shape controllability of scaffolds. Six samples (1–6) were analyzed over 21 days of culture (Scale bar: 500 µm). (f) Area [$mm^2$] and diameter (average of diameter in X- and Y-direction) [mm] were conducted with image analysis using ImageJ, $n = 6$; statistical significance was calculated via One-way ANOVA and Tukey´s multiple comparison test. **g**, Metabolic activity assessment of six independent samples over a culture period of 10 days (alamarBlue assay, $n = 3$ technical replicates per data point).



15214095, 0, Downloaded from https://advanced.onlinelibrary.wiley.com/doi/10.1002/adma.75116, Wiley Online Library on [27/09/2026]. See the Terms and Conditions (https://onlinelibrary.wiley.com/terms-and-conditions) on Wiley Online Library for rules of use; OA articles are governed by the applicable Creative Commons License

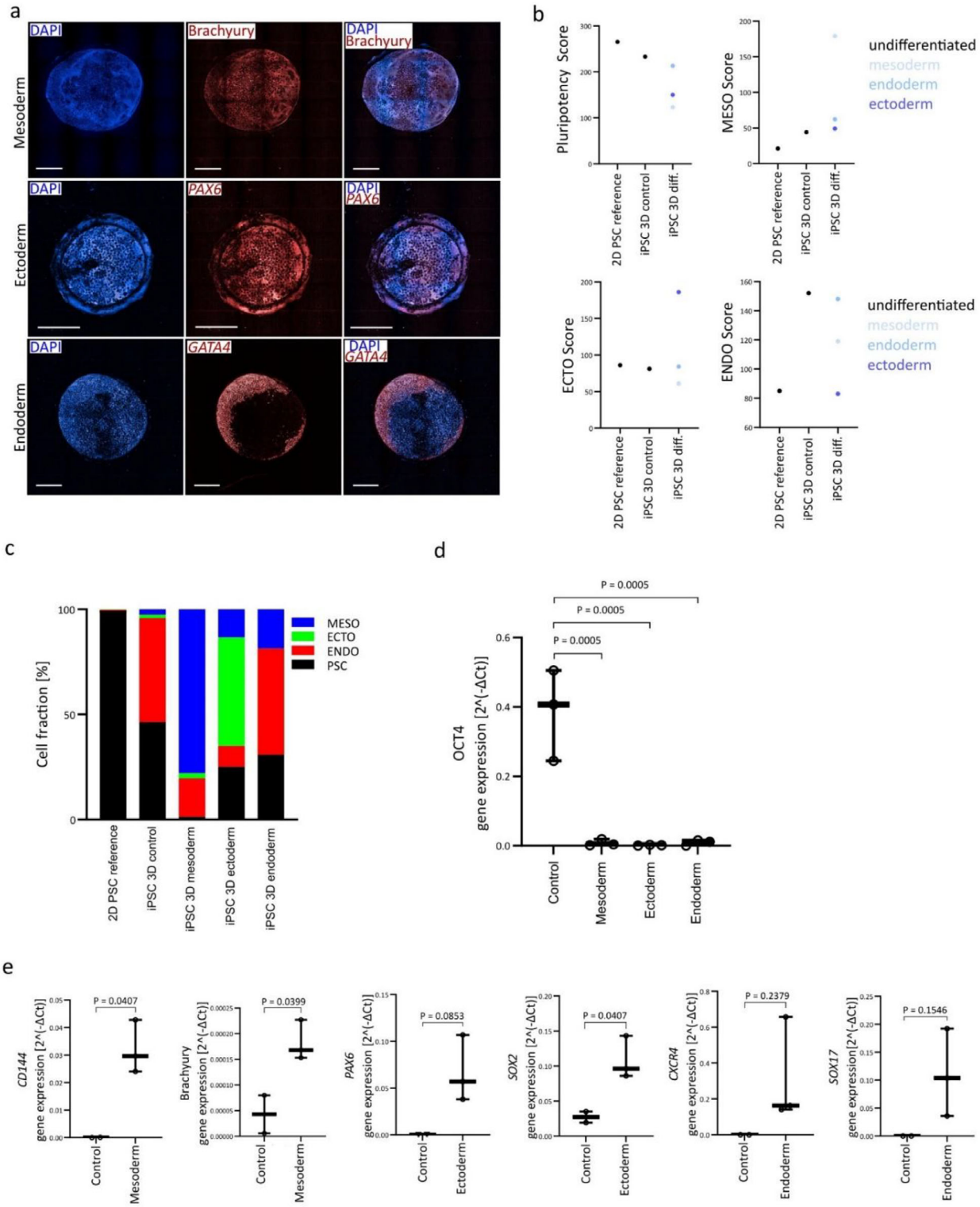



**FIGURE 3** | Differentiation potential of iPSC/microgel scaffolds into the three germ layers. (a) Immunostaining of germ layer-specific markers after 7 days of directed differentiation (scale bar is 2 mm, DAPI (blue)). Endoderm (*GATA4* (red), confocal Z-stack images (666 μm)), ectoderm *(PAX6* (red), confocal Z-stack images (740 μm)), mesoderm (Brachyury (red), confocal Z-stack images (814 μm)). (b) Pluripotency and differentiation scores inside scaffolds after 7 days of directed differentiation for three conditions: iPSC 2D reference (data from [50]), iPSC undifferentiated control (3D), iPSC differentiated samples (3D). (c) Deconvolution of methylation data against reference matrix (data from [50]) demonstrating the different cell fractions in each sample. (d) RT–qPCR of pluripotency marker OCT4 after 7 days of directed differentiation into each germ layer. Gene expression values were calculated using the $2^{-\Delta Ct}$- method, and statistical significance was calculated via One-way ANOVA and Tukey´s multiple comparison test (control $n = 2$, sample: $n = 3$; each $n$ includes four pooled biological replicates). (e) RT–qPCR of germ layer-specific markers (endoderm*: CXCR4*, *SOX17*, ectoderm*: PAX6*, *SOX2*, mesoderm: *CD144*, Brachyury). Gene expression values were calculated using the $2^{-\Delta Ct}$- method, and statistical significance was calculated via unpaired *t*-tests (control $n = 2$, sample $n = 3$; each $n$ includes four pooled biological replicates.).



15214095, 0, Downloaded from https://advanced.onlinelibrary.wiley.com/doi/10.1002/adma.75116, Wiley Online Library on [27/09/2026]. See the Terms and Conditions (https://onlinelibrary.wiley.com/terms-and-conditions) on Wiley Online Library for rules of use; OA articles are governed by the applicable Creative Commons License

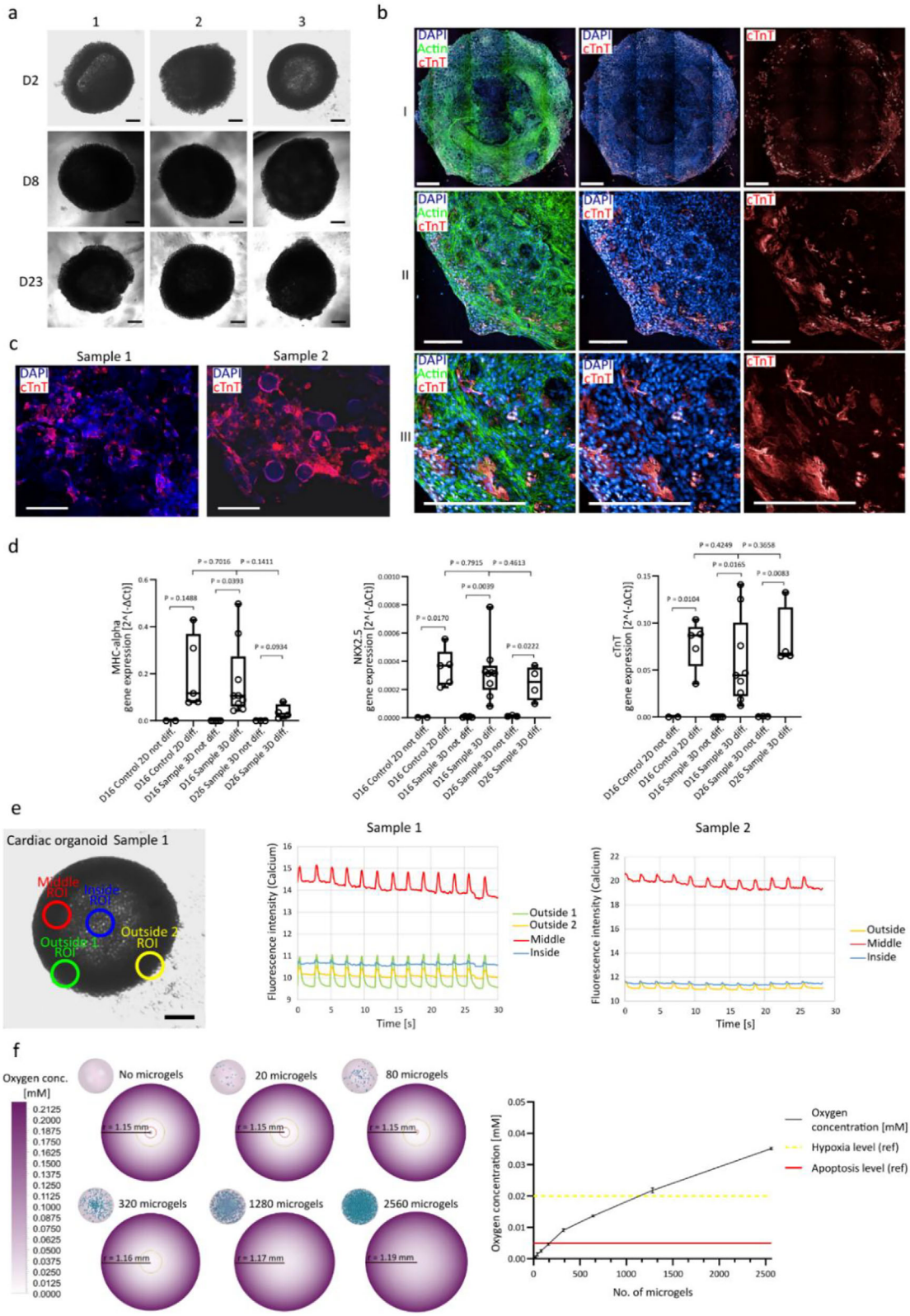



**FIGURE 4** | Differentiation into cardiac organoids. (a) Uniform shape of cardiac organoids over 23 days of culture (3 different samples (1–3); scale bar is 1 mm). (b) Immunofluorescence confocal imaging of cardiac organoids on day 23 of culture (DAPI (blue), Actin (Phalloidin, green), cTnT (red)). Confocal Z-stack images (720 μm); scale bar 1 is 1 mm, and 2 and 3 are 200 μm. (c) Cryosections from the middle (Z-axis) of cardiac organoids on day 23. Cryosections were stained for DAPI (blue) and cTnT (red), demonstrating cardiac differentiation inside the construct. Scale bars are 200 μm. (d) RT–qPCR of cardiac-specific markers (*MHC-alpha*, *NKX2.5*, *cTnT*) on day 16 and day 26 of differentiation with respective undifferentiated controls and a 2D comparison. Gene expression values were calculated using the $2^{-\Delta Ct}$- method, and statistical significance was calculated via unpaired *t*-tests ($n = 3$ – $n = 9$; each $n$ includes four pooled biological replicates). (e) Calcium imaging of cardiac organoids (performed at one Z-plane). The different



15214095, 0, Downloaded from https://advanced.onlinelibrary.wiley.com/doi/10.1002/adma.75116, Wiley Online Library on [27/09/2026]. See the Terms and Conditions (https://onlinelibrary.wiley.com/terms-and-conditions) on Wiley Online Library for rules of use; OA articles are governed by the applicable Creative Commons License

successful differentiation throughout the mm-sized organoid. The reduced cTnT signal observed in the center of the maximum projection confocal images (Figure 4b) results from fluorescence intensity loss due to the samples' density. While the edges can be imaged without significant attenuation across the entire Z-stack, the central regions experience signal reduction because of the limited laser penetration depth. Consequently, the maximum projection appears with higher fluorescence intensity at the edges compared to the center. The inside of the organoids was, therefore, analyzed with cryosections, displaying cell nuclei and cTnT expression, demonstrating cardiac differentiation and cell nuclei in the scaffold core (Figure 4c). We validated cardiac differentiation with RT–qPCR of the marker genes *MHC-alpha*, *NKX2.5*, and *cTnT* at days 16 and 26 of differentiation. The 3D cardiac organoids demonstrated comparable marker gene expression to the two-dimensional control culture, disproving possible negative effects of the microgel-containing scaffold on cardiac differentiation. Furthermore, we observed a decrease in *MHC-alpha* [51] and *NKX2.5* [52] expression alongside an increase in *cTnT* expression [53] from day 16 to day 26 of differentiation, both suggesting the beginning maturation of cardiomyocytes (Figure 4d). The cardiac organoids proved functional through consistent, uniform beating, demonstrating their inherent pacemaker properties and the formation of an interconnected network throughout the whole scaffold (Videos S1 and S2). Calcium imaging within distinct regions of interest (ROIs) across the cardiac organoids exhibited equivalent beating frequencies, validating the cardiomyocyte interconnectivity without hindrance by the microgels (Figure 4e). These results suggest the successful formation of mm-sized cardiac organoids using iPSCs-microgels-based scaffolds.

To further evaluate the potential role of microgels in improving oxygen transport inside the scaffolds, we simulated oxygen diffusion inside cardiomyocyte spheroids containing 600 000 cells, which is estimated to be comparable scope as the experiment after proliferation. The oxygen diffusion within the microgel-supported scaffold was investigated through numerical simulations based on the transport diffusion equation. The steady-state oxygen concentration profiles were obtained by solving the governing partial differential equation using a finite volume method. The simulation suggested an increase in oxygen concentration throughout the scaffold with increasing microgel amount (Figure 4f). With approximately 1,280 microgels added, the formation of a necrotic core ($C_{Oxygen} < 0.005$ mM [54]) and hypoxic area (0.005 mM $< C_{Oxygen} <$ 0.02 mM [55]) could theoretically be circumvented. These results supported the hypothesis that microgels may improve oxygen transport within large dense scaffolds. Thereby, the simulation supports our observation that with an even higher number of microgels (4335 microgels/scaffold), we could generate mm-sized cardiac organoids with improved oxygen diffusion. However, since this conclusion is mainly based on simulation data, further experimental studies are required in the future.

### 1.4 | Scale-Down of Scaffold Production to 96-Well Format and Differentiation to Cardiac Organoids and Retinal Photoreceptor Cells

We scaled down the proposed microgel platform for iPSC expansion and differentiation to a 96-well format, allowing for smaller scaffold production with higher throughput. While the above-described mm-scale scaffolds required a centrifugation step to ensure stable microgel-iPSC scaffolds that could be transferred from conical tubes into 24-well plates, the reduced initial cell numbers (100 000 cells) enabled stable scaffold formation through gravitational settling within U-shaped 96-well plates. The reduction of the initial cell number was compatible with a 96-well plate regarding media volume. The 96-well U-shaped well plates were employed without the necessity of centrifugation, simplifying the process and avoiding unnecessary strain on the cells (Figure 5a). Although, here the experiments performed in this format were all handled manually, and demonstrates the facile use in many laboratories without automated pipetting systems, the absence of a centrifugation step would, in principle, facilitate the usage of this workflow in an automated setup. After 48 h of iPSC expansion inside the microgel-based scaffolds (337 cells/microgel), the cells were differentiated into stable cardiac organoids. This cell/microgel ratio is higher than for the mm-scale organoids, likely due to the fact that no centrifugation step is included. The cross-section of the organoids had an area of 0.96 ± 0.13 $mm^2$ (Figure S7), which is a reduction in size of approximately 3.5-fold compared to the millimeter-size scaffolds (Figure 2f). Figure 5b shows a single microgel as a representative view of the uniform cell monolayer covering the microgel surface, indicating a strong cell-material interaction. Cardiac differentiation was confirmed via immunofluorescence staining (cTnT) throughout the whole scaffold and uniform beating across the organoids (Figure 5c; Videos S4 and S5). The cTnT fibers are directly adjacent to the microgels arranged around the microgel surface (Figure 5d), and generate characteristic striations, implying that the microgels support the formation of a functional and interconnected cTnT network (Figure 5e).

As a demonstration of the applicability of this scaffold approach for different tissues, we also differentiated the constructs into retinal lineage cells expressing photoreceptor-associated markers. The iPSC-based microgel scaffolds (185 cells/microgel) were assembled, and we initiated the differentiation by adapting a 2D photoreceptor differentiation protocol to our 3D system [56]. The cell/microgel ratio here differs from the one applied for cardiac

ROIs (outside, middle, inside) were set and analyzed with NIS Elements software, demonstrating consistent cardiomyocyte contraction frequency (fluorescence intensity changes) at the respective ROIs. Left image: general positioning of ROIs respective to cardiac organoid (sample 1) (scale bar is 500 μm). Right: graphs representing calcium imaging data in each of the ROIs for two samples. (f) Simulation results of oxygen transport. Left: contour plots of oxygen concentration. Simulation of oxygen transport in a cardiac organoid with a 1.15 mm radius shows the formation of a necrotic core ($C_{Oxygen} < 0.005$ mM) and hypoxic area (0.005 mM $< C_{Oxygen} <$ 0.02 mM). Right: correlation between minimal oxygen concentration and microgel volume ratio determined through simulation. Further details regarding oxygen transport modeling and simulation and a comparison to an iPSC-microgel scaffold (Figure S6) are reported in supplementary and methods.



15214095, 0, Downloaded from https://advanced.onlinelibrary.wiley.com/doi/10.1002/adma.75116, Wiley Online Library on [27/09/2026]. See the Terms and Conditions (https://onlinelibrary.wiley.com/terms-and-conditions) on Wiley Online Library for rules of use; OA articles are governed by the applicable Creative Commons License

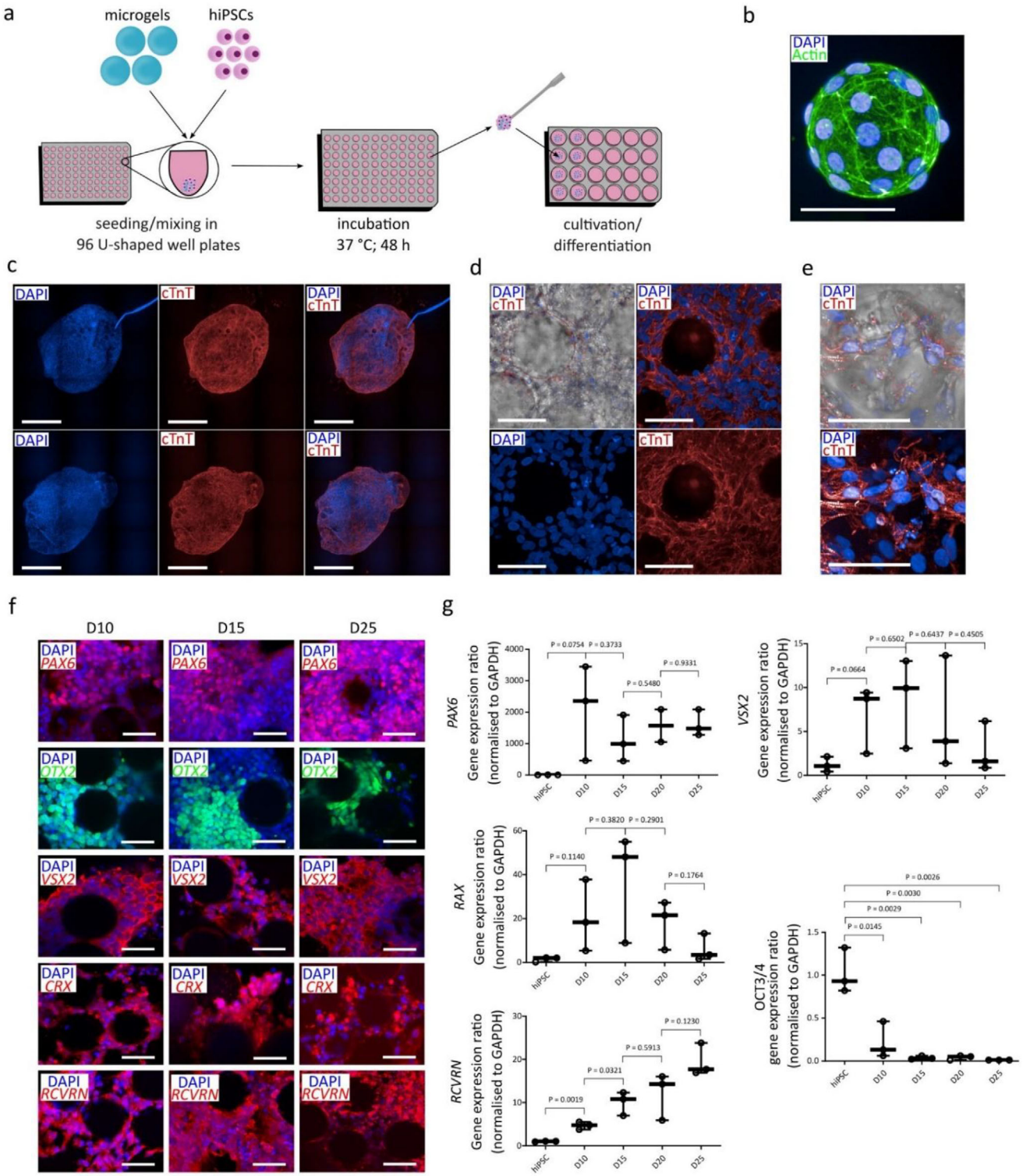



**FIGURE 5** | Scale-down of scaffold production and differentiation. (a) Schematic illustration of iPSCs/microgels scaffold production in a 96-well plate (prepared with Inkscape). (b) Single microgel with a cell monolayer broken of the scaffold during staining after 30 days stained for Actin (green) and DAPI (blue). Scale bar is 50 μm. (c) Immunofluorescence confocal imaging of cardiac organoids on day 30 of culture, stained with DAPI (blue) and for cTnT (red). Confocal Z-stack images (540 μm), scale bar is 500 μm. (d) Immunofluorescence images of microgels embedded in cardiac organoid. Confocal Z-stack images (30 μm) and the scale bar is 50 μm. (e) Immunofluorescence images of distinct cTnT structure in cardiomyocytes surrounding a microgel inside a cardiac organoid. Confocal Z-stack images (200 μm) and the scale bar is 50 μm. (f) Immunofluorescence images of retinal differentiation of scaffold with distinct retinal markers (PAX6 (red), OTX2 (green), VSX2 (red), CRX (red), RCVRN (red)) on day 10, 15, and 25 of culture. Confocal Z-stack images (29-114 μm) and the scale bar is 50 μm. (g) RT–qPCR of retinal differentiation (*PAX6*, *VSX2*, *RAX*, *RCVRN*) and pluripotency markers (*OCT3/4*). Gene expression ratios were calculated with a script provided by TopTipBio and statistical significance was calculated via unpaired t-tests ($n = 3$).



15214095, 0, Downloaded from https://advanced.onlinelibrary.wiley.com/doi/10.1002/adma.75116, Wiley Online Library on [27/09/2026]. See the Terms and Conditions (https://onlinelibrary.wiley.com/terms-and-conditions) on Wiley Online Library for rules of use; OA articles are governed by the applicable Creative Commons License

organoids, since a higher initial cell number was used for retinal photoreceptor differentiation. With higher cell numbers, the proliferation-related increase in cells is higher than with lower starting cell numbers, while the microgel amount stays constant. We observed thereby, that the lower the initial cell number used, the higher the cell/microgel ratio should be for the formation of stable scaffolds within 48 h using this seeding method. Throughout the differentiation process, we observed key milestones in photoreceptor development. Retinal cells were characterized at various stages by immunofluorescence microscopy and qRT–PCR (Figure 5f,g). By day 10, there was a notable increase in the expression of eye field transcription factors *PAX6* and *RAX* compared to undifferentiated iPSCs. Furthermore, we detected *VSX2*, a marker specific to retinal progenitor cells, and *CRX*, a marker of photoreceptor progenitors. *CRX* expression first observed in the microgel scaffold at day 10 occurs earlier than reported in retinal organoids and photoreceptor differentiation protocols from iPSCs, which were described to take at least 21 days [56–59]. This earlier differentiation is likely due to the 3D system, which provides a more conducive environment, along with the physiological stiffness of the microgels compared to tissue culture plastic. The expression of recoverin, a calcium-binding protein crucial for phototransduction, increased consistently over the course of 25 days.

Using the U-shaped 96-well plates, we demonstrated successful differentiation of the expanded iPSCs inside the microgel scaffolds into two different targets, illustrating the applicability of the proposed technology for variable use in organoid and stem cell research.

### 1.5 | High-Throughput Production of iPSCs/Microgels Scaffolds Using an Automated Liquid Handling System

After establishing the iPSC-microgel technology for the 96-well plate format, the next objective was to apply the proposed system in an automated liquid handling system for high-throughput automated production of 3D constructs with potential application for compound screening. We developed a method to enable the formation of iPSC/microgel scaffolds for organoid formation in low-volume (25 µL) flat surface 384-well plates (Figure 6a). The scaffold formation in this manner is solely driven by the self-assembly of the iPSCs with the microgels into 3D spherical constructs. This cell-driven assembly was highly dependent on the cell-to-microgel ratio, which was optimized to allow for the formation of one single scaffold per well (Videos S6–S10). Figure S8a demonstrates how iPSCs use microgels at different cell-to-microgel ratios to assemble into sizable spherical structures in a fully automated workflow. Based on stability and shape of the iPSC/microgel scaffolds, a ratio of 125 cells/microgel was selected with 10 000 iPSCs and 80 microgels (Figure S8a). We observed good scaffold formation and the lowest number of dead cells or non-incorporated microgels for this condition. The increase in the cell number to more than 20.000 per sample caused an increase in cell debris, indicating cell death of non-incorporated iPSCs. For this ratio, we observed the formation of spherical scaffolds after 24 h, with a subsequent stabilizing and densifying of the construct within 48 h, resulting in an average area of 0.19 ± 0.05 $mm^2$. The size of the scaffolds increased consistently up to an area of 0.25 ± 0.03 $mm^2$ after 5 days of culture, pointing out iPSC expansion in a high cell-density scaffold (Figure 6e,f). Additionally, the possibility of scaffold transfer through automated pipetting was demonstrated, allowing for the removal of cell debris during culture time (Figure S8), needed for an optimized culture workflow. This last step is essential for the automated handling of the organoids during long-term culture. We observed microgels incorporated and distributed throughout the scaffold (Figure 6d). Furthermore, we demonstrated the applicability of this method for a large number of samples (160) in an automated manner, depicting the potential for large-scale organoid production or drug screenings in the future (Figure S9).

To validate the compatibility of the high-throughput system for iPSC-based applications, the pluripotency of the automatically produced scaffolds was confirmed after 48 h by immunostaining for OCT4 (Figure 6e). Mean grey value analysis of the confocal DAPI and OCT4 stained images exhibited low standard deviations of 4.6% (DAPI) and 7.4% (OCT4), indicating reproducible cell numbers of pluripotent cells (Figure 6e). Furthermore, OCT4 expression, as an indicator for pluripotent state, was similar in cells directly adjacent to the microgels with cell-material contact as compared to cells further away from a microgel, only experiencing cell-cell contacts. We thereby conclude that iPSCs and microgels, processed by the automated pipetting system, also form 3D constructs with iPSCs maintaining pluripotency. To demonstrate the applicability of the high-throughput system for organoid production, we generated cardiac organoids by inducing cardiac differentiation after 48 h of scaffold formation under iPSC maintenance conditions. After 30 days of differentiation, we observed spontaneously beating (Video S11) cardiac organoids, which furthermore expressed cardiac Troponin T (cTnT) homogeneously throughout the whole scaffold (Figures 6g,i). The mean grey value analysis of DAPI and cTnT expression in these organoids demonstrated reproducibility of the production and a reproducible differentiation (Figure 6h). Figure 6j additionally demonstrates the uniform differentiation of cardiac organoids without reduced differentiation towards the center of the organoid.

Additionally, to further characterize our cardiac organoid platform, we established calcium imaging and high-speed bright-field (BF) imaging to assess spontaneous contractile activity. To overcome the technical limitations associated with low-volume 384-well plates, we continued using standard U-bottom 384-well plates, which provide a larger culture medium volume and improved long-term culture conditions. Figure 7a shows the morphological development of a representative cardiac organoid over 30 days of culture. Calcium imaging of the same organoid at day 24 demonstrates coordinated calcium transients associated with spontaneous contractions (Figure 7b). A representative beating trace obtained from another organoid at day 30 is shown in Figure 7c, exhibiting 12 contraction peaks over a 20 s recording period (0.6 Hz). The proportion of beating organoids increased progressively during differentiation, reaching 96% of organoids with measurable recordings after day 20 of culture (Figure 7e). Some wells were not recorded (yellow bar) due to occasional autofocus failures during automated acquisition of the well plate. Beating frequency was subsequently quantified at multiple time



15214095, 0, Downloaded from https://advanced.onlinelibrary.wiley.com/doi/10.1002/adma.75116, Wiley Online Library on [27/09/2026]. See the Terms and Conditions (https://onlinelibrary.wiley.com/terms-and-conditions) on Wiley Online Library for rules of use; OA articles are governed by the applicable Creative Commons License

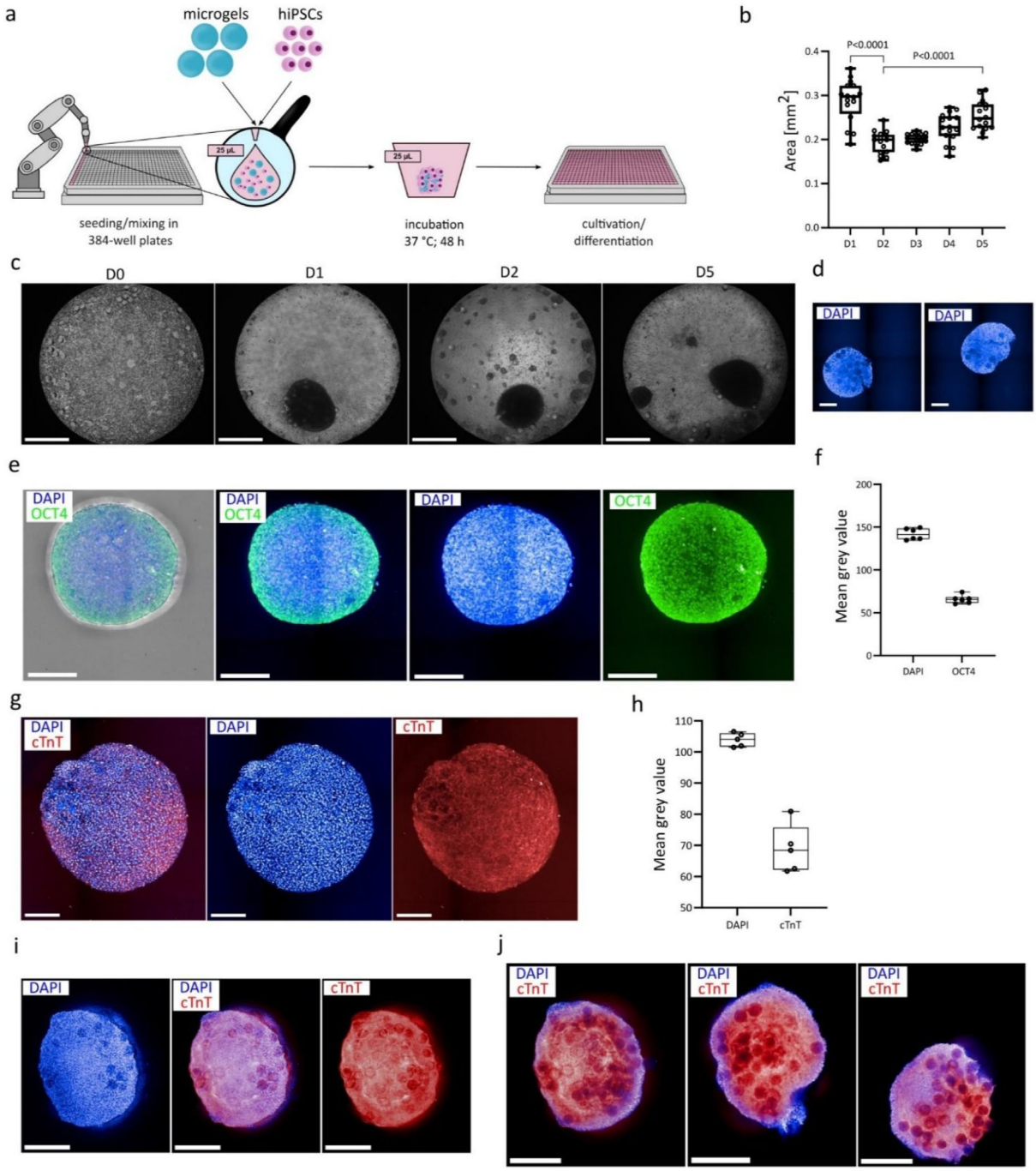
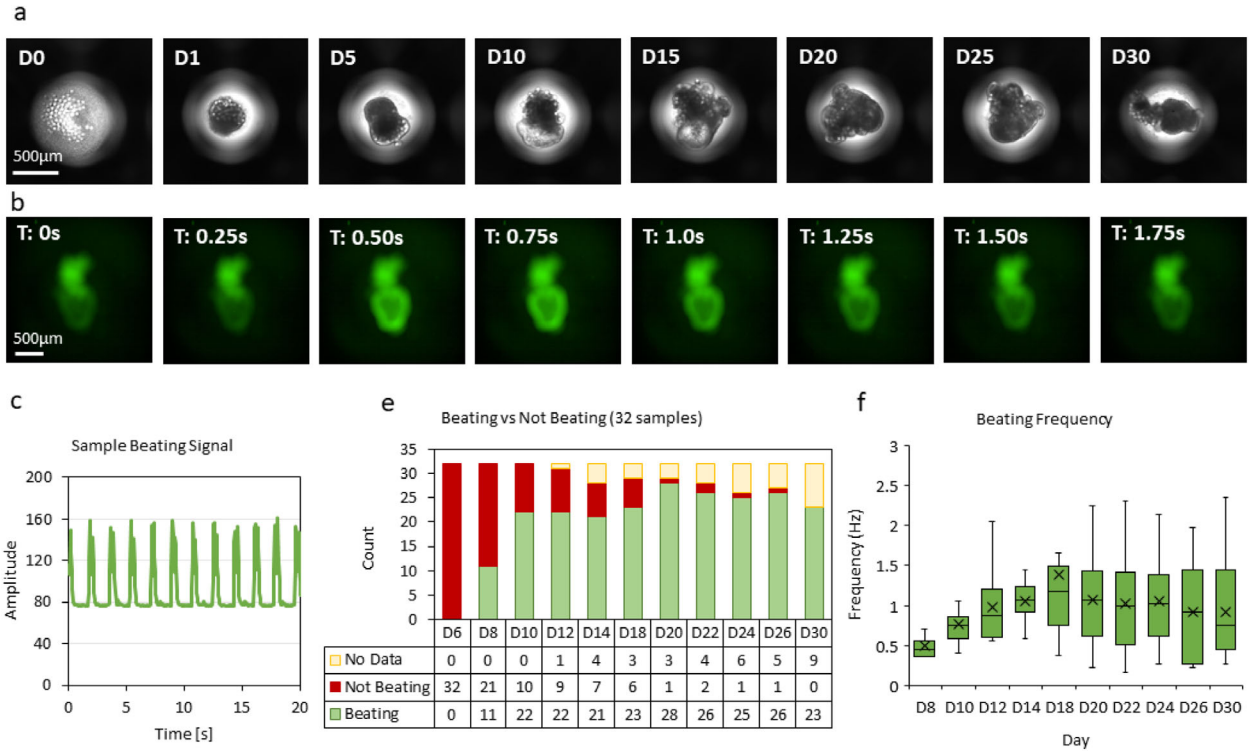



**FIGURE 6** | Automated production of scaffolds. (a) Schematic illustration of iPSCs/microgels scaffold production method inside 384-well plates (prepared with Inkscape) using an automated liquid handling system. (b) Scaffold area analysis over 5 days of culture. Compaction of scaffolds from first to second day with subsequent scaffold growth. Statistical significance was calculated via One-way ANOVA and Tukey´s multiple comparison test ($n = 16$). (c) Scaffold formation and culture in low-volume 384-well plates at day 0, 1, 2, and 5 (scale bar: 500 µm). (d) Middle view of the scaffold after 2 days of culture (DAPI (blue)). Scale bar: 200 µm. Left image: segment (37 µm) from the middle of the Z-stack image (324 µm). Right image: segment (18 µm) from the middle of the Z-stack image (333 µm). (e) Pluripotency of scaffolds after 2 days (DAPI (blue), OCT4 (green)). Scale bar: 200 µm. Confocal Z-stack (288 µm). Mean grey values of DAPI and OCT4 stains in scaffolds at day 2. Low standard deviation demonstrated reproducible cell number and pluripotency for automated scaffold production. (f) Mean grey values of DAPI and OCT4 stains in scaffolds at day 2. Low standard deviation demonstrated reproducible cell number and pluripotency for automated scaffold production ($n = 6$). (g) Cardiac differentiation of scaffolds day 30 (DAPI (blue), cardiac Troponin T (cTnT) (red)); Confocal Z-stack images at 10x magnification (296 µm) (scale bar: 200 µm). (h) Mean grey values of DAPI and cTnT stains in scaffolds at day 30. Low standard deviation demonstrated reproducible cell number and differentiation for automated scaffold production ($n = 5$). (i) Cardiac differentiation of scaffolds day 30, a clearing protocol was used to visualize microgels inside of the constructs; (DAPI (blue), cardiac Troponin T (cTnT) (red)); Confocal Z-stack images 10x magnification (296 µm) (scale bar: 200 µm). (j) Single plane at 59.2 µm depth of cardiac differentiated scaffolds for the demonstration of microgel distribution throughout the construct and uniform differentiation. (DAPI (blue), cardiac Troponin T (cTnT) (red)); Confocal Z-stack images 10x magnification (296 µm) (scale bar: 200 µm).



15214095, 0, Downloaded from https://advanced.onlinelibrary.wiley.com/doi/10.1002/adma.75116, Wiley Online Library on [27/09/2026]. See the Terms and Conditions (https://onlinelibrary.wiley.com/terms-and-conditions) on Wiley Online Library for rules of use; OA articles are governed by the applicable Creative Commons License




| | D6 | D8 | D10 | D12 | D14 | D18 | D20 | D22 | D24 | D26 | D30 |
|---|---|---|---|---|---|---|---|---|---|---|---|
| No Data | 0 | 0 | 0 | 1 | 4 | 3 | 3 | 4 | 6 | 5 | 9 |
| Not Beating | 32 | 21 | 10 | 9 | 7 | 6 | 1 | 2 | 1 | 1 | 0 |
| Beating | 0 | 11 | 22 | 22 | 21 | 23 | 28 | 26 | 25 | 26 | 23 |

**FIGURE 7** | Characterization of spontaneous contractile activity in cardiac organoids using bright-field and calcium imaging. (a) Representative bright-field images showing the morphological development of a cardiac organoid during 30 days of differentiation (scale bar: 500 µm). (b) Representative calcium imaging sequence of the same organoid at day 24, illustrating spontaneous calcium transients associated with coordinated contractions. Time is indicated in the upper left corner of each frame (scale bar: 500 µm). (c) Representative contractile trace obtained by high-speed bright-field imaging from a day 30 cardiac organoid, showing spontaneous beating activity over a 20 s recording. (e) Quantification of the proportion of beating and non-beating cardiac organoids at different stages of differentiation ($n = 32$ organoids). Yellow bars indicate samples for which beating could not be assessed due to missing or unusable recordings (e.g., occasional autofocus failures during automated acquisition of the well plate. Among organoids with measurable recordings, spontaneous beating increased during differentiation and reached 96% after day 20 of culture. (f) Distribution of spontaneous beating frequencies measured at the indicated differentiation time points. Box plots show the median (horizontal line), interquartile range (box), and minimum and maximum values (whiskers), with the mean indicated by ×.

points throughout differentiation, demonstrating maturation of spontaneous contractile activity over time (Figure 7f).

These results demonstrate that microgel-iPSC scaffolds can be generated in an automated 384-well format and support cardiac differentiation under the tested conditions, indicating potential for future adaptation to high-throughput organoid production workflows including drug discovery or disease modeling.

## 2 | Conclusion

In stem cell and organoid research, challenges regarding reproducibility and scalability prevail, complicating the reliable application of these technologies for drug development and disease modeling. To tackle some of these challenges, we have developed a new technology that combines iPSC expansion and differentiation within the same construct and facilitates the reproducible manufacturing of organoids from sizable to high-throughput. This approach is entirely chemically defined, employing PEG-based microgels, coated with recombinantly produced vitronectin, as the matrix material, and using xeno-free media. The reproducibility of the platform was supported by uniform microgel production, a constant microgel production rate, defined cell-to-microgel ratios for each workflow, and microgel number determination using a volume-based calibration curve. Under the optimized conditions, scaffold formation was consistently observed in the mm-scale, 96-well, and automated 384-well formats. We believe that this technology can provide a user-friendly foundation for advancing chemically defined organoid and stem cell research for many different tissue models with a significant impact on tissue engineering and pharmacology. Application of more specialized microgel systems, which allow for introducing features such as larger pore sizes [39, 40], mechanical actuation [60], and alignment [61] for controlling tissue architecture and differentiation, is among the interesting opportunities to be embedded into this technology. Additionally, the incorporation of the microgels could be further developed to allow for morphogen release [62] or structural gradient formation [63], proposing a potential for the generation of spatially defined compartments within one organoid. These advancements could open up a wide range of new possibilities for organoid development and maturation, enabling more relevant models that could better recapitulate native tissue architecture and lead to more mature organoids. The scalability and reproducibility of the method could furthermore aid in long-term cultivation [64] and complex patterning [63], contributing to advancements in disease modelling and



15214095, 0, Downloaded from https://advanced.onlinelibrary.wiley.com/doi/10.1002/adma.75116, Wiley Online Library on [27/09/2026]. See the Terms and Conditions (https://onlinelibrary.wiley.com/terms-and-conditions) on Wiley Online Library for rules of use; OA articles are governed by the applicable Creative Commons License

high-throughput drug screening. Most approaches for long-term cultivation or mm-scale organoids require additional handling steps, for example, organoid slicing or stirring cultures to allow for the needed nutrient and oxygen supply [65, 66], which can complicate direct integration into automated workflows. Furthermore, the platform demonstrates adaptability to different tissue types, proposing a potential in supporting structural and functional aspects across diverse biomedical applications. These findings demonstrate the material characteristics and workflow possibilities of the microgel-based platform for use with iPSCs, providing a platform for future application-specific comparative studies with established organoid culture systems. Depending on the specific application, the microgel properties, such as stiffness, visco-elasticity, porosity, dimensions, shape, and coating, can be varied in a systematic and chemically-defined manner. In the long term, we believe this platform could serve as a modular foundation for building complex, mature, functional tissue systems suitable for translational research. Future research must further tune these materials for specific tissue types, which requires close collaboration between stem cell researchers and materials scientists. The insights gained from this research could bring organoid studies closer to reducing or replacing animal testing, while also providing human-based alternatives to improve and accelerate drug development and personalized medicine in the future.

## 3 | Materials and Methods

### 3.1 | Microfluidic Master Mold Fabrication

A positive 3D structure of the microfluidic channel geometry was designed (AutoCAD 2019), processed in DeScribe 2.7, and fabricated using two-photon direct laser writing (Nanoscribe GmbH, Photonic Professional GT). As previously described [67], an acrylsilanized glass coverslip (LABSOLUTE Th. Geyer 76 × 26 × 1 mm) was covered with a photoresist (Nanoscribe, IP-S) and mounted in the 3D printer. The print was performed with a 25x objective (Blocksize X: 200 Y: 200 Z: 160 µm, Shear 15°). After printing completion, the master structure was submerged in propylene glycol monomethyl ether acetate (PGMEA, Sigma-Aldrich, ≥ 99.5%) for 10 min to remove uncrosslinked polymer resin, followed by washing with isopropanol (IPA) solution for 3 min. The substrate was dried under nitrogen flow and post-cured for 4–6 h using UV light (200 mW, $\lambda$ = 365 nm). The cured structure was fluorosilanized with trichloro-(1H,1H,2H,2H-perfluoroctyl)-silane (50 µL per glass coverslip) in a desiccator under high vacuum overnight.

### 3.2 | Microfluidic Chip Fabrication

A mixture of PDMS base and curing agent (10:1 w/w, Sylgard 184, Dow Corning) was cast on the master structure, degassed, and cured at 60°C for 12 h. The PDMS replica was cut from the master mold, inlet holes were punched (0.75 mm biopsy puncher, Electron Microscopy Science), and cleaned with IPA and Milli-Q water. The glass slide (76 × 52 × 1 mm, Marienfeld, Germany) was prepared analogously, including additional washing steps with acetone. The PDMS slab and glass slide were plasma-treated (PVA TePla 100 Plasma System, 28 mL/min $O_2$, 100 W, 40 s) and bonded together. The microfluidic chip was stored at 60°C for 12 h to complete the bonding. Before use, the device was rendered hydrophobic by chemical vapor deposition (CVD) with trichloro-(1H,1H,2H,2H-perfluoroctyl)-silane (50 µL per chip) in a vacuum desiccator overnight. Afterward, the outside of the chip was rinsed with Novec 7500 (3 M) and wiped using lint-free tissues.

### 3.3 | Microgel Production

Epoxy-functionalized microgels were prepared from aqueous solutions composed of polyethylene glycol diacrylate (PEG-DA, 15% w/w, Mn 700, Sigma–Aldrich), Lithium-Phenyl-2,4,6-trimethylbenzoylphosphinate (LAP, 1% w/w, Sigma–Aldrich) photoinitiator, and freshly distilled glycidyl methacrylate (GMA, 1% w/w, Sigma–Aldrich). As a control, unfunctionalized PEG microgels were produced analogously without the addition of GMA. The solution was stored in brown glass vials until use to protect from undesired light exposure. The continuous oil phase was composed of Novec HFE 7500 with Krytox 157 FSH surfactant (4.5% v/v, DuPont). Both solutions were transferred into a syringe (Hamilton Gastight Series 1000, 10 mL), and the syringe containing the dispersed phase was wrapped in aluminum foil. A 25G cannula was inserted into PTFE tubing (OD 0.9 mm, ID 0.4 mm, TECHLAB GmbH) and attached to the syringes. Residual air was removed, and the syringes were fixed in a syringe pump (Havard Apparatus Pump 11 Elite). The other ends of the tubes, as well as an outlet tube (Polyethylene, OD 0.038 in, ID 0.023 in, Instech Laboratories), were inserted into the dedicated inlet holes on the microfluidic device. The continuous phase was started at a flow rate of 1000 µL/h to prefill the collection reservoir. Afterwards, the dispersed phase was started at 1000 µL/h until droplet formation was visible. The flow rates were then adjusted to 3000 and 2000 µL/h for the continuous and dispersed phases, respectively. Droplet crosslinking was achieved by guiding the outlet tube through a self-constructed UV–LED set-up, as previously reported [68]. Briefly, the UV set-up contains a fixed frame featuring an array of five LEDs (Starboard, Luminus SST-10-UV-A130, 365 nm) spaced at a distance of 23 mm, powered by a 24 V power supply, and operating at an irradiation dose of 30.36 mW/cm$^2$. The microgels are crosslinked in-flow by fixing the outlet tube in a PDMS gasket connected to the frame. Purification of the microgels was achieved by multiple subsequent washing steps, as previously reported [69]. In short, the excess continuous phase was pipetted off, and the microgels were sequentially washed with Novec HFE 7500, n-hexane + span 80 (1% v/v), n-hexane, IPA, and Milli-Q water. Each solvent was applied five times before proceeding to the next solvent. After the purification, the microgels were stored in Milli-Q water at 4°C until use.

### 3.4 | Epoxide Labeling With Fluoresceinamine-Isomer I and Qualitative Confocal Imaging

Incorporation of GMA was qualitatively analyzed by amine-epoxide coupling with fluoresceinamine-isomer I. Fluoresceinamine in DMSO (5 mg/ml, 100 µL) was added



15214095, 0, Downloaded from https://advanced.onlinelibrary.wiley.com/doi/10.1002/adma.75116, Wiley Online Library on [27/09/2026]. See the Terms and Conditions (https://onlinelibrary.wiley.com/terms-and-conditions) on Wiley Online Library for rules of use; OA articles are governed by the applicable Creative Commons License

in excess to a dispersion of PEG-DA-co-GMA and PEG-DA microgels in water (30 µL jammed microgel sediment, 900 µL Milli-Q water), yielding a final fluoresceinamine concentration of 0.5 mg/ml. Amine-epoxy coupling was achieved overnight on a roller. The microgels were then washed twice with DMSO and six times with Milli-Q water to remove excess unbound fluoresceinamine. Confocal laser scanning microscopy was performed on a Leica TCS SP8 microscope (Leica Microsystems, Germany). Fluoresceinamine was excited at $\lambda$ = 488 nm via an argon laser. The HC PL FLUOTAR 10x/0.30 DRY objective was used to detect the resulting emission at $\lambda$ = 500–555 nm.

### 3.5 | Nanoindentation

The mechanical properties of the microgel particles were determined using a Pavone Nanoindenter (Optics11Life, Amsterdam, The Netherlands) equipped with a cantilever-based analysis probe with a spherical tip radius of 10 µm and a cantilever stiffness of 0.48 N/m. Prior to measurement, 40 µL of microgel dispersion was pipetted into a 24-well plate, followed by the addition of 1 mL buffered solution, as indicated. To ensure attachment of the microgels to the well plate surfaces, the well plate bottom was pre-treated overnight with a poly-L-lysine solution (50 µL, 0.1% w/v in water, Sigma–Aldrich). All measurements were performed at room temperature. The microgel particles were indented p to a maximum load of 1.2 µN and a piezo speed of 1 µm/s. The obtained load-indentation curves were used to calculate the effective Young's modulus using the Hertzian contact model, fitted to a maximum indentation depth of 1600 nm. The data analysis was performed with Dataviewer V 2.5 (Optics11Life).

### 3.6 | Vitronectin-Functionalization of Microgels

Prior to functionalization with vitronectin, the microgels, suspended in 1x PBS pH 7.4, were UV-sterilized for 2 h and subsequently handled only under sterile conditions. Microgels were functionalized with the Vitronectin XF solution (STEMCELL technologies). Therefore, microgels were pelleted and resuspended in an equal volume of 1xPBS corresponding to the pellet volume (e.g., 100 µL microgel pellet + 100 µL 1x PBS). To this, equal volumes of the VTN solution (e.g., 100 µL) at a concentration of 250 µg/mL were added, reaching a final concentration of 125 µg/mL. The final solution was incubated overnight at 4°C and for 20 min at 37°C directly prior to use for experiments.

### 3.7 | Cell Culture

Two iPSC lines (UKAi009-A and UKAi0011-A) were used in this study, and further information can be found in the Human Pluripotent Stem Cell Registry (hPSCreg) [70]. Maintenance cell culture of iPSCs was performed in tissue culture-treated 6-well plates coated with Vitronectin (Vitronectin XF STEMCELL technologies,# 07180; 0.5 µg/cm$^2$) in StemMACS iPS-Brew XF (Miltenyi biotec, 130-104-368). Cells used during this work were between passages 18 and 53.

### 3.8 | Differentiation Into Three Germ Layers

Germlayer differentiation was performed on scaffolds on day 2 using the StemMACS Trilineage Differentiation Kit (Miltenyi biotec, 130-115-660), yielding fully differentiated samples after 7 days (endoderm 5 days of differentiation) of differentiation according to the supplier protocol. After 7 days of differentiation (9 days of culture), samples were further analyzed by RT–qPCR, epigenetic analysis, or immunofluorescence staining.

### 3.9 | Differentiation Into Cardiac Organoids

Cardiac organoid differentiation was performed starting after 48 h of scaffold formation using the StemMACS CardioDiff Kit XF (Miltenyi biotec, 130-125-289). Media were prepared as described in the protocol. Time points of mesoderm and cardiac induction were applied as described in the protocol, while media changes were performed daily for the whole culture time, differing from the protocol provided by the supplier. Cardiac organoid culture was performed for different culture periods ranging from 16 to 31 days. Samples were further analyzed by RT–qPCR and immunofluorescence staining after culture.

### 3.10 | Differentiation of iPSCs to Photoreceptor Progenitors

Human induced pluripotent stem cells (iPSC-106) were cultured on vitronectin (STEMCELL technologies)-coated tissue culture plate. After reaching 70%–80% confluency, the iPSCs were seeded with microgels in a 96-well ultra-low attachment U-bottom plate and maintained in iPS-Brew medium (Miltenyi Biotec) for 48 h to promote embryoid body (EB) formation. Retinal differentiation was performed based on a published protocol with suitable modifications [56]. Unlike the published protocol, EBs were maintained in suspension culture throughout differentiation rather than plating them onto Matrigel-coated surfaces. Retinal induction was initiated by replacing the iPS-Brew medium with Retinal Induction Medium (RIM), which consisted of DMEM/F12 (Gibco), 10% KSR (Gibco), 0.1 mM nonessential amino acids (Sigma), 1% N2 (Gibco), 2% B27 without vitamin A (Gibco), supplemented with 10 ng/mL Noggin (STEMCELL Technologies), 10 ng/mL DKK 1 (STEMCELL Technologies), 10 ng/mL IGF-1 (R&D Systems), and 5 ng/mL basic fibroblast growth factor (bFGF; Millipore). After 5 days, the medium was replaced with RIM without KSR, and the cultures were maintained under 3D suspension conditions until day 25.

### 3.11 | Assessment of Vitronectin-Functionalization

The VTN-functionalized microgels (description above) were pelleted, and 25 µL of pellet volume was pipetted into a 96-well plate. Afterward, 200.000 iPSCs (1000 cells/µL) were added to each well, and iPS-Brew was used as the media. For the first 24 h, 10 µM of ROCK inhibitor (Y-27632 (Dihydrochloride), STEMCELL technologies, # 72304) was added. Media was exchanged daily, and after 4 days of culture, the cell-material interaction was assessed via brightfield microscopy.



15214095, 0, Downloaded from https://advanced.onlinelibrary.wiley.com/doi/10.1002/adma.75116, Wiley Online Library on [27/09/2026]. See the Terms and Conditions (https://onlinelibrary.wiley.com/terms-and-conditions) on Wiley Online Library for rules of use; OA articles are governed by the applicable Creative Commons License

### 3.12 | Microgel-iPSC Scaffold Formation

After reaching around 80% confluency, iPSCs were detached into single cells using ACCUTASE (STEMCELL technologies, # 07920) cell detachment solution. Afterwards, microgels stored in the coating solution were centrifuged (1 min, RT, 8000 rpm) and the coating solution was replaced with iPS-Brew media, in a ratio of 4:1 media to microgel pellet volume (e.g., 400 µL media + 100 µL microgel pellet). The respective microgel number added to the experiments using this microgel solution was calculated using a calibration curve (Figure S3). To all prepared experiments, ROCK-inhibitor (Y-27632 (Dihydrochloride), STEMCELL technologies, # 72304) was added at a concentration of 10 µM for the first 24 h.

### 3.13 | mm-Scale Scaffolds

For the preparation of mm-scale scaffolds, 100 µL microgel solution (explained above) and 400.000 cells (1000 cells/µL) were added to a 1.5 mL protein LoBind Eppendorf tube and filled with iPS-Brew media to a volume of 800 µL. Afterwards, the mixture was put on the Stuart SSM3 mini gyro-rocker at 16 rpm (angles between 5° and 12°) for 1 h inside the incubator (37°C, 5% $CO_2$) to allow for initial attachment of the cells to the microgels. Subsequently, the mixture was centrifuged for 4 min at 300 g (RT), and the resulting pellets were cultured for 48 h inside the Eppendorf tubes in the incubator, with a 700 µL media exchange after 24 h. On the second day, formed scaffolds were removed from the tubes using a small spatula and transferred into 24-well plates filled with 500 µL media per well. They were either cultured in iPS-Brew media or differentiated (see below) with daily media change.

### 3.14 | 96-Well Plate Scaffold Production

Either 6.25 µL (maintenance and cardiac differentiation) or 25 µL (retinal differentiation) microgel solution was pipetted into Nunclon Sphera U-well 96-well plates (Thermo–Fisher scientific, 174925) with 100.000 cells (maintenance and cardiac differentiation) or 200.000 cells (retinal differentiation), respectively. The volume was filled up to 250 µL per well, and 200 µL of iPS-Brew media was changed after 24 h. On the second day, the formed scaffolds were transferred into 24/48-well plates using a small spatula and cultured either in maintenance or differentiation media (see below) with daily media change (500 µL).

### 3.15 | Scaffold Production in 384-Well Plate With Automated Liquid Handling System

JANUS G3 automated liquid handling workstations (Revvity, USA) were used for automated production of scaffolds in high-throughput format. All aspiration, dispensing, and mixing procedures were performed using the Varispan dispensing arm. A 384 low-volume plate (Greiner Bio-One, Netherlands) was used. Initially, the above-described microgel solution and a cell solution with a concentration of $5 \times 10^6$ cells/mL were prepared in two separate 1.5 mL Eppendorf tubes (protein low-bind in case of microgels), which were used with the automated liquid handling system to prepare a master mix of cells and microgels in a third Eppendorf tube. Each well was filled with 5.25 µL of cell-microgel master mix (1.25 µL microgel solution, 4 µL cell solution) and 19.75 µL iPS-Brew media. To minimize evaporation from experimental wells, adjacent wells to the experimental ones were filled with 25 µL 1x PBS. After one day of culture, the cells and microgels self-assembled into an organoid-like scaffold lying on the bottom of the well plate. Then, the daily media change was performed by discarding 17 µL of old media from the top of the well using the liquid tracking option. The wells were then filled with the same volume of new culture media. Note that each step requires proper aspiration and/or dispensing vertical position with respect to the bottom of the wells and proper liquid tracking setup to ensure precise dispensing/aspiration and avoid cross-contamination and bubble formation. Additionally, we were able to transfer the organoid from well to well, hence removing cell debris by gently aspirating 15 µL at 1 mm above the well bottom and dispensing it in a new well using an automated liquid handling system.

### 3.16 | Immunostaining and Fixation of Scaffolds

Scaffolds were fixed with 4% PFA for 45 min and afterward washed with 1x PBS pH 7.4 for three times and afterward incubated in a solution containing 4% BSA (SEQENS) and 0.1% Triton X-100 (Sigma–Aldrich) for 1 h to permeabilize the cell membrane and blocking. Before the staining procedure, samples were washed three times with PBS. Phalloidin 488 stain was incubated for 3 h (RT) at a dilution of 1:1000 in PBS (Phalloidin-iFluor 488 Reagent, abcam, (ab176753)). Afterwards, samples were incubated with DAPI stain (1:500 in PBS) for 10 min (RT) and washed 4 times with PBS. Pluripotency staining for OCT4 was performed with the Oct3/4 primary antibody (Santa Cruz, sc-5279) at a concentration of 1:200 overnight at 4°C. Afterward, samples were washed 2 times with PBS and incubated with the secondary antibody Alexa Fluor 488, 594, or 633 for 1 h at RT, with subsequent DAPI staining (above) or direct washing 3 times with PBS. The germlayer-specific primary antibody stains were used in the following concentrations: Brachyury (RandD systems, AF2085) 1:20; GATA6 (Cell Signaling Technology, #5851) 1:1000; PAX6 (RandD systems, AF8150) 1:100. Cardiac-specific staining for cardiac Troponin T was performed with the primary cTnT antibody (biotechne, MAB18741-100) in a concentration of 1:200. Secondary antibodies and DAPI stains were applied as described before. Samples were stored in 1x PBS at 4°C prior to imaging. Some samples were additionally incubated in a tissue clearing solution for 24 h and imaged in the respective solution (Ultrapure water: 40 % D-Sorbitol, 10% Glycerol, 4 M Urea, 0.2% Triton X-100, 15% DMSO) [71]. All confocal images were recorded using the Opera Phoenix Confocal microscope (revvity).

### 3.17 | Immunofluorescence Staining (Photoreceptor progenitors)

Scaffolds were fixed with 4% paraformaldehyde at 4°C for 30 min. Samples were permeabilized with 0.3% Triton X-100 for 20 min at room temperature. 1% BSA in PBS was used for blocking. Samples were then incubated overnight at 4°C with primary antibody in 1% BSA solution containing 0.1% Triton X-100. After washing three times, 10 min each, the secondary



15214095, 0, Downloaded from https://advanced.onlinelibrary.wiley.com/doi/10.1002/adma.75116, Wiley Online Library on [27/09/2026]. See the Terms and Conditions (https://onlinelibrary.wiley.com/terms-and-conditions) on Wiley Online Library for rules of use; OA articles are governed by the applicable Creative Commons License

antibody diluted in PBS containing 0.1% Triton X-100 solution was added to the samples and incubated overnight at 4°C. Samples were washed three times, 10 min each, before imaging with a laser scanning microscope. Primary antibodies used were: PAX6 (GenTex-Biozol GTX113241), OTX2 (R&D Systems BAF1979), VSX2 (Sigma–Aldrich AB9016), CRX (R&D Systems, AF7085), Recoverin (Millipore, AB5585-1). Secondary antibodies used were: AF594 anti-rabbit IgG (H+L) (Invitrogen A11012), AF594 anti-sheep IgG (H+L) (Abcam AB150180), AF555 anti-goat IgG (H+L) (Invitrogen (Life Technologies), A21432).

### 3.18 | Clearing Protocol (Used for High-Throughput Experiments)

An alternative clearing protocol was applied for the automatically produced samples, since the lack of airflow inside the automated pipetting system does not allow for the use of hazardous chemicals. This protocol was adapted from the user protocol UP11 by ibidi. After immunostaining was performed as described above, samples will be incubated in an increasing dilution series of Isopropanol, performed on ice. Add 30% Isopropanol (diluted with distilled water) and incubate the samples for 15 min on ice. Repeat this step consecutively with Isopropanol dilutions of 50% and 70%. Afterwards, incubate the samples in pure isopropanol for 15 min and repeat this step once. The samples have to be heated to room temperature afterwards, before the addition of Ethyl cinnamate (Sigma–Aldrich, CAS: 103-36-6). Incubate the sample in pure Ethyl cinnamate (99%) for 30 min to 1 h before imaging. Samples will be imaged in Ethyl cinnamate.

### 3.19 | Cryocutting and Staining of Slices

The samples were fixed in 4% PFA as described above. After washing with 1x PBS, samples were embedded in liquid OCT solution (Cellpath, KMA-0100-00A) in cryomolds (Sakura, $10 \times 10 \times 5\text{mm}^3$, Ref 4565). Samples were incubated in OCT for 1 h before shock freezing. Shock freezing was done by placing a beaker with n-pentane into liquid nitrogen; afterwards, the cryomolds were placed into the n-pentane until the sample was completely frozen. Frozen cryomolds were stored overnight at –20°C. Cryocutting of samples was performed with a cryotome, Leica CM1950. The samples were cut into 5 µm slices throughout the whole sample to determine the middle area for analysis. Slices were stored on glass slides at -20°C. Immunostaining was performed on the slices as follows: First, slices were placed in –20°C cold acetone for 10 min then they were dried and placed into MilliQ water for 10 min afterward. Staining afterwards was performed in a humidified Petri dish using the same time points and concentrations as described above. After immunostaining, samples were mounted using DPX Mountant (Sigma–Aldrich). Imaging was performed using the ECHO Revolution (ECHO a BICO company) microscope.

### 3.20 | Live/Dead Staining of Scaffolds

Viability assessment was performed after 2 days of culture ($n = 3$) using the LIVE/DEAD Cell Imaging Kit (Invitrogen). The scaffolds were stained according to the protocol provided by the supplier and imaged using the Opera Phoenix Confocal microscope with a 10×/N.A. 0.3 air objective (revvity).

### 3.21 | Image Analysis

The image analysis of fluorescence intensity and maximum projection analysis was performed using the Harmony software (revvity). Further image analysis was conducted with the ImageJ software. Area analysis of scaffolds was performed, generating a 16-bit image, converting this image into a binary image using the default threshold method, and subsequently measuring the white pixel area. Diameter analysis was performed by applying the arrow tool for freehand measurements. Confocal image fluorescence intensity was analyzed by measuring the mean grey values of 16-bit converted maximum projection Z-Stack images.

### 3.22 | Epigenetic Analysis of Germ Layer Differentiation

Pluripotent state and three lineage differentiation potential of iPSCs were analyzed by cell-type specific DNA methylation changes using PluripotencyScreen, as described in detail before [50]. The genomic DNA was isolated from the samples using the NucleoSpin Tissue Kit (Macherey-Nagel, 740952.50), and the yielded DNA was afterwards quantified with the NanoDrop 2000 spectrophotometer (Thermo Fisher Scientific). Bisulfite conversion of the genomic DNA was performed overnight using 500 ng DNA with the EZ DNA Methylation Kit (Zymo Research, D5002), and the elution was performed in 20 µL elution buffer. The PyroMark PCR Kit (Qiagen, ID. 978801) was used to amplify the target sequences using 2.5 mM $Mg^{2+}$ and a primer concentration of 0.3 µm. Afterwards, targeted DNA methylation analysis was performed by pyrosequencing on a Q96PyroMark Q48 Autoprep Instrument (Qiagen) for three CG dinucleotides (CpGs) with characteristic modifications in the pluripotent state, mesoderm, endoderm, and ectoderm. The results can be used for deconvolution to estimate proportions of cellular differentiation toward these lineages. The primers for PCR and pyrosequencing can be found in Table S2.

### 3.23 | Metabolic Activity Assay

The metabolic activity analysis was performed using the alamarBlue reagent (Invitrogen) in the recommended concentration of 1:10 in iPS-Brew media. The samples ($n = 6$) were incubated in 500 µL of the Resazurin solution for 2 h at 37°C in the incubator. Afterwards, 50 µL of the solution was transferred into a 96-well plate ($n = 3$) and fluorescence was measured with a fluorescence plate reader (Tecan) according to the supplied protocol (emission: 590 nm; excitation: 530 nm).

### 3.24 | RT–qPCR

Immediately after culture, samples were lysed using the RLT-lysis buffer supplied with the RNeasy Mini Kit (Qiagen, 74104) and stored at -80°C until further use. Prior to RNA-Isolation, lysed samples were homogenized using QIAshredder columns



15214095, 0, Downloaded from https://advanced.onlinelibrary.wiley.com/doi/10.1002/adma.75116, Wiley Online Library on [27/09/2026]. See the Terms and Conditions (https://onlinelibrary.wiley.com/terms-and-conditions) on Wiley Online Library for rules of use; OA articles are governed by the applicable Creative Commons License

(Qiagen, 79656) to remove the microgels from the lysis solution. Subsequently, RNA isolation was performed with the RNeasy Mini Kit (Qiagen, 74104), and concentration and purity were measured with NanoDrop UV/VIS Spectrophotometer. cDNA conversion was performed with 300–1000 ng of mRNA through application of the PrimeScript RT Master Mix (Takara Bio, RR036A) according to the protocol. RT-qPCR was performed with the SsoAdvanced Universal SYBR Green Supermix (BioRad) on the CFX96 Touch Real-Time PCR Detection System (BioRad). As a reference gene, GAPDH was applied, and analysis was done using the $2^{(-\Delta Ct)}$- method. All utilized primers can be found in Table S1.

### 3.25 | RT–qPCR (photoreceptor progenitors)

Total RNA was extracted using RNeasy kit (Qiagen). For each sample, 1 µg of RNA was reverse transcribed using a cDNA synthesis kit (Qiagen). All results were confirmed by three independent biological samples at each data point. Primers are listed in the Table S1.

### 3.26 | Calcium Imaging and Video Analysis of Cardiac Organoids

Calcium imaging was performed according to the protocol described by Y. Yao et al. [72]. Therefore, samples were stained with 4 µM Fluo4-AM diluted in 1x PowerLoad (Invitrogen, P10020) for 30 min. Afterward, samples were washed and calcium imaging was performed in calcium imaging buffer (in MilliQ water: 137 mM NaCl, 1.5 mM $CaCl_2$, 5.4 mM KCl, 0.44 mM $KH_2PO_4$, 0.5 mM $MgCl_2$, 0.4 mM $MgSO_4$, 0.3 mM $Na_2HPO_4$, 0.4 mM $NaHCO_3$, 5.6 mM D-Glucose, 10 mM HEPES at pH 7.4). Calcium imaging analysis was performed using the NIS elements imaging software and the Nikon Eclipse Ti2-e microscope. The same microscope setup was used for the recording of the cardiac organoid beating videos.

### 3.27 | Simulation of Oxygen Diffusion in Scaffolds

Ansys CFX 2023 R1 was used to simulate oxygen transport within the organoids. This software uses the element-based finite volume method to solve numerically the governing equations. We idealized the organoid geometry as a fully spherical construct consisting of a continuum of cellular material and the microgels distributed within it. Stationary domains with no fluid flow were considered for both microgels and cells. The microgels' positions within the organoids were generated by an IronPython script using normalized random number generation. The script checks if the distance between the microgels is greater than 2×r, where r is the radius of the microgel. For each condition, three randomly generated microgel distributions were obtained. The cells were modeled as a continuum material with defined cell density ($1 \times 10^{14}$ cells $m^{-3}$), oxygen diffusion coefficient ($1 \times 10^{-9}$ $m^2$ $s^{-1}$), and oxygen consumption rate ($2 \times 10^{-18}$ mol $cell^{-1}$ $s^{-1}$ for iPSCs and $1 \times 10^{-17}$ mol $cell^{-1}$ $s^{-1}$ for cardiomyocytes). The oxygen diffusion coefficient within the microgels was set to $2.5 \times 10^{-9}$ $m^2$ $s^{-1}$. The oxygen concentration around the organoid was set to 0.22 mM. An isothermal condition was imposed, and the maximum root mean square (RMS) residual error of $10^{-6}$ was used as the convergence criterion for the transport equation. The grid study was performed to ensure that the proper element size was used, and a steady-state simulation was considered. Ansys CFX uses the equation below as the mathematical model for the simulation of oxygen transport within the stationary domains.

$$\frac{\partial(\Phi)}{\partial t} = \nabla.(D\,\nabla\Phi) + S_\Phi$$

where, $\Phi$, $D$ and $S_\Phi$ are the oxygen concentration, kinematic diffusivity and volumetric source term.

### 3.28 | Automated Beating Analysis Using Bright Field Images

In a controlled imaging environment, the total pixel intensity within a fixed frame should remain constant if the subject is static. However, as a heart organoid contracts and relaxes, there will be edge displacement as the borders of the organoid move in and out. Furthermore, the physical deformation of the tissue results in thickness changes, which modulate light absorption and intensity. By measuring the mean intensity across the 400 frames, a time-series signal is created where each dip or peak corresponds to a phase of the cardiac cycle (systole or diastole). This turns a 2D video into a 1D oscillation, making it suitable for mathematical analysis. The intensity of an organoid over 400 frames is a discrete signal. To find the rhythms, the discrete Fourier transform (DFT) is applied via the FFT algorithm. When the results of the FFT are plotted, a power spectrum is derived. Each peak on this graph represents a specific frequency that is physically present in the organoid's motion. The peaks in this spectrum tell which frequencies are most dominant in the organoid's movement.

To identify beating organoids, a threshold was set based on the amplitude of the intensity signal. This threshold was determined by visually comparing the recorded videos with the corresponding data peaks for a set of selected organoids. Organoids with an amplitude higher than this value were classified as beating and included in the analysis, while those failing below it were categorized as nonbeating.

### 3.29 | Statistical Analysis

Statistical analysis and graphs were produced using Prism software. Box plots represent boxes and whiskers from minimal to maximal values, including all data points. The performed statistical analysis for each data set is reported in the respective figure caption. For statistical analysis, the *p*-values were represented in the figures.

#### Author Contributions

**Aaron Babendreyer**: methodology, resources. **Laura Klasen**: conceptualization, investigation, writing – original draft, methodology, validation, visualization, writing – review and editing, formal analysis, data curation. **Matthias Mork**: conceptualization, investigation, writing – original



15214095, 0, Downloaded from https://advanced.onlinelibrary.wiley.com/doi/10.1002/adma.75116, Wiley Online Library on [27/09/2026]. See the Terms and Conditions (https://onlinelibrary.wiley.com/terms-and-conditions) on Wiley Online Library for rules of use; OA articles are governed by the applicable Creative Commons License

draft, methodology, validation, visualization, writing – review and editing, formal analysis, data curation. **Ramin Nasehi**: investigation, methodology, writing – review and editing, validation, software, formal analysis, visualization, data curation. **Laura De Laporte**: conceptualization, funding acquisition, writing – review and editing, project administration, supervision, resources. **Wolfgang Wagner**: writing – review and editing, resources, supervision, funding acquisition. **Kira Zeevaert**: writing – review and editing, methodology. **Jacopo Di Russo**: investigation, writing – review and editing, supervision, resources. **Vasudha Turuvekere Krishnamurthy**: methodology, validation, visualization, writing – review and editing, data curation, formal analysis.


## Acknowledgements

The authors gratefully acknowledge funding from the European Research Council within the ERC-2021-COG project 101043656, Heartbeat. We gratefully acknowledge funding from the German Research Foundation (DFG) within the project C3 and C9N of the Collaborative Research Centre (CRC 985) "Functional Microgels and Microgel Systems", AnisoMatic IGF 01IF23480N, and the Research Training Group Mechanobiology in Epithelial 3D Tissue Constructs (ME3T; 363055819/GRK2415). Furthermore, this work was supported through funding from the Senatsausschuss Wettbewerb (SAW) Leibniz-Transfer project µTISSUEfab and Leibniz Health Technologies Short Term Scientific Mission (STSM) funding, and by the Federal Ministry of Education and Research (VIP+: PluripotencyScreen; 03VP11580), as well as the Exploratory Research Space (ERS) Seed Fund G:(DE-82)EXS-SF-SFASIA004. The authors thank Greta Romahn for her contribution in preparing microgels via microfluidics, Paphassorn Karoon-ngampun for her help with the high-throughput experiment maintenance and preparation, and Céline Bastard for her help with cell culture and experiment maintenance.

Open access funding enabled and organized by Projekt DEAL.


## Conflicts of Interest

Wolfgang Wagner and Kira Zeevaert are involved in Cygenia GmbH (www.cygenia.com), which can provide services for epigenetic characterization of cell preparations to other scientists.

## Data Availability Statement

The data that support the findings of this study are available from the corresponding author upon reasonable request.

## References


1. M. Huch, J. A. Knoblich, M. P. Lutolf, and A. Martinez-Arias, "The Hope and the Hype of Organoid Research," *Development* 144, no. 6 (2017): 938–941, https://doi.org/10.1242/dev.150201.

2. J. G. Camp, K. Sekine, T. Gerber, et al., "Multilineage Communication Regulates Human Liver Bud Development From Pluripotency," *Nature* 546, no. 7659 (2017): 533–538, https://doi.org/10.1038/nature22796.

3. F. Sampaziotis, M. Cardoso de Brito, P. Madrigal, et al., "Cholangiocytes Derived From Human Induced Pluripotent Stem Cells for Disease Modeling and Drug Validation," *Nature Biotechnology* 33, no. 8 (2015): 845–852, https://doi.org/10.1038/nbt.3275.

4. T. Takebe, K. Sekine, M. Enomura, et al., "Vascularized and Functional Human Liver From an iPSC-Derived Organ Bud Transplant," *Nature* 499, no. 7459 (2013): 481–484, https://doi.org/10.1038/nature12271.

5. L. Drakhlis, S. Biswanath, C.-M. Farr, et al., "Human Heart-Forming Organoids Recapitulate Early Heart and Foregut Development," *Nature Biotechnology* 39, no. 6 (2021): 737–746, https://doi.org/10.1038/s41587-021-00815-9.

6. Y. R. Lewis-Israeli, A. H. Wasserman, M. A. Gabalski, et al., "Self-Assembling Human Heart Organoids for the Modeling of Cardiac Development and Congenital Heart Disease," *Nature Communications* 12, no. 1 (2021): 5142, https://doi.org/10.1038/s41467-021-25329-5.

7. B. Volmert, A. Kiselev, A. Juhong, et al., "A Patterned Human Primitive Heart Organoid Model Generated by Pluripotent Stem Cell Self-Organization," *Nature Communications* 14, no. 1 (2023): 8245, https://doi.org/10.1038/s41467-023-43999-1.

8. J. A. Bagley, D. Reumann, S. Bian, J. Lévi-Strauss, and J. A. Knoblich, "Fused Cerebral Organoids Model Interactions Between Brain Regions," *Nature Methods* 14, no. 7 (2017): 743–751, https://doi.org/10.1038/nmeth.4304.

9. F. Birey, J. Andersen, C. D. Makinson, et al., "Assembly of Functionally Integrated Human Forebrain Spheroids," *Nature* 545, no. 7652 (2017): 54–59, https://doi.org/10.1038/nature22330.

10. M. A. Lancaster, M. Renner, C.-A. Martin, et al., "Cerebral Organoids Model Human Brain Development and Microcephaly," *Nature* 501, no. 7467 (2013): 373–379, https://doi.org/10.1038/nature12517.

11. M. Eiraku, N. Takata, H. Ishibashi, et al., "Self-Organizing Optic-Cup Morphogenesis in Three-Dimensional Culture," *Nature* 472, no. 7341 (2011): 51–56, https://doi.org/10.1038/nature09941.

12. S. Reichman, A. Terray, A. Slembrouck, et al., "From Confluent Human iPS Cells to Self-Forming Neural Retina and Retinal Pigmented Epithelium," *Proceedings of the National Academy of Sciences* 111, no. 23 (2014): 8518–8523, https://doi.org/10.1073/pnas.1324212111.

13. G. Liang and Y. Zhang, "Embryonic Stem Cell and Induced Pluripotent Stem Cell: An Epigenetic Perspective," *Cell Research* 23, no. 1 (2013): 49–69, https://doi.org/10.1038/cr.2012.175.

14. J. J. Vandana, C. Manrique, L. A. Lacko, and S. Chen, "Human Pluripotent-stem-Cell-Derived Organoids for Drug Discovery and Evaluation," *Cell Stem Cell* 30, no. 5 (2023): 571–591, https://doi.org/10.1016/j.stem.2023.04.011.

15. Y.-S. Hwang, B. G. Chung, D. Ortmann, N. Hattori, H.-C. Moeller, and A. Khademhosseini, "Microwell-Mediated Control of Embryoid Body Size Regulates Embryonic Stem Cell Fate via Differential Expression of WNT5a and WNT11," *Proceedings of the National Academy of Sciences* 106, no. 40 (2009): 16978–16983, https://doi.org/10.1073/pnas.0905550106.

16. P. Hoang and Z. Ma, "Biomaterial-Guided Stem Cell Organoid Engineering for Modeling Development and Diseases," *Acta Biomaterialia* 132 (2021): 23–36, https://doi.org/10.1016/j.actbio.2021.01.026.

17. P. S. Thakuri, C. Liu, G. D. Luker, and H. Tavana, "Biomaterials-Based Approaches to Tumor Spheroid and Organoid Modeling," *Advanced Healthcare Materials* 7, no. 6 (2018): 1700980, https://doi.org/10.1002/adhm.201700980.

18. A. Abdul Samat and B. H. Yahaya, "Biomaterials in Organoid Development," in *Organoid Technology for Disease Modelling and Personalized Treatment*, ed. B. H. Yahaya, (Springer International Publishing, 2022), 155–178, https://doi.org/10.1007/978-3-030-93056-1_8.

19. C. S. Hughes, L. M. Postovit, and G. A. Lajoie, "Matrigel: A Complex Protein Mixture Required for Optimal Growth of Cell Culture," *Proteomics* 10, no. 9 (2010): 1886–1890, https://doi.org/10.1002/pmic.200900758.

20. N. Sachs, Y. Tsukamoto, P. Kujala, P. J. Peters, and H. Clevers, "Intestinal Epithelial Organoids Fuse to Form Self-Organizing Tubes in Floating Collagen Gels," *Development* 144, no. 6 (2017): 1107–1112, https://doi.org/10.1242/dev.143933.

21. J. H. Jee, et al., "Development of Collagen-Based 3D Matrix for Gastrointestinal Tract-Derived Organoid Culture," *Stem Cells International* 1 (2019): 8472712.

22. V. Magno, A. Meinhardt, and C. Werner, "Polymer Hydrogels to Guide Organotypic and Organoid Cultures," *Advanced Functional Materials* 30, no. 48 (2020): 2000097, https://doi.org/10.1002/adfm.202000097.

23. N. Broguiere, L. Isenmann, C. Hirt, et al., "Growth of Epithelial Organoids in a Defined Hydrogel," *Advanced Materials* 30, no. 43 (2018): 1801621, https://doi.org/10.1002/adma.201801621.

24. D. Wang, Y. Guo, J. Zhu, et al., "Hyaluronic Acid Methacrylate/Pancreatic Extracellular Matrix as a Potential 3D Printing Bioink





15214095, 0, Downloaded from https://advanced.onlinelibrary.wiley.com/doi/10.1002/adma.75116, Wiley Online Library on [27/09/2026]. See the Terms and Conditions (https://onlinelibrary.wiley.com/terms-and-conditions) on Wiley Online Library for rules of use; OA articles are governed by the applicable Creative Commons License

for Constructing Islet Organoids," *Acta Biomaterialia* 165 (2023): 86–101, https://doi.org/10.1016/j.actbio.2022.06.036.

25. G. G. Giobbe, C. Crowley, C. Luni, et al., "Extracellular Matrix Hydrogel Derived From Decellularized Tissues Enables Endodermal Organoid Culture," *Nature Communications* 10, no. 1 (2019): 5658, https://doi.org/10.1038/s41467-019-13605-4.

26. J. W. Kim, S. A. Nam, J. Yi, et al., "Kidney Decellularized Extracellular Matrix Enhanced the Vascularization and Maturation of Human Kidney Organoids," *Advanced Science* 9, no. 15 (2022): 2103526, https://doi.org/10.1002/advs.202103526.

27. L. Varinelli, M. Guaglio, S. Brich, et al., "Decellularized Extracellular Matrix as Scaffold for Cancer Organoid Cultures of Colorectal Peritoneal Metastases," *Journal of Molecular Cell Biology* 14, no. 11 (2023): 1–14, https://doi.org/10.1093/jmcb/mjac064.

28. N. Gjorevski, N. Sachs, A. Manfrin, et al., "Designer Matrices for Intestinal Stem Cell and Organoid Culture," *Nature* 539, no. 7630 (2016): 560–564, https://doi.org/10.1038/nature20168.

29. M. T. Kozlowski, C. J. Crook, and H. T. Ku, "Towards Organoid Culture Without Matrigel," *Communications Biology* 4, no. 1 (2021): 1387.

30. Z. Gan, X. Qin, H. Liu, J. Liu, and J. Qin, "Recent Advances in Defined Hydrogels in Organoid Research," *Bioactive Materials* 28 (2023): 386–401.

31. V. Hernandez-Gordillo, T. Kassis, A. Lampejo, et al., "Fully Synthetic Matrices for In Vitro Culture of Primary Human Intestinal Enteroids and Endometrial Organoids," *Biomaterials* 254 (2020): 120125, https://doi.org/10.1016/j.biomaterials.2020.120125.

32. S. S. Ng, K. Saeb-Parsy, S. J. I. Blackford, et al., "Human iPS Derived Progenitors Bioengineered into Liver Organoids Using an Inverted Colloidal Crystal Poly (Ethylene Glycol) Scaffold," *Biomaterials* 182 (2018): 299–311, https://doi.org/10.1016/j.biomaterials.2018.07.043.

33. R. Goetzke, H. Keijdener, J. Franzen, et al., "Differentiation of Induced Pluripotent Stem Cells Towards Mesenchymal Stromal Cells Is Hampered by Culture in 3D Hydrogels," *Scientific Reports* 9, no. 1 (2019): 15578, https://doi.org/10.1038/s41598-019-51911-5.

34. B. L. Ekerdt, C. M. Fuentes, Y. Lei, et al., "Thermoreversible Hyaluronic Acid-PNIPAAm Hydrogel Systems for 3D Stem Cell Culture," *Advanced Healthcare Materials* 7, no. 12 (2018): 1800225, https://doi.org/10.1002/adhm.201800225.

35. C. M. Madl, B. L. LeSavage, R. E. Dewi, et al., "Maintenance of Neural Progenitor Cell Stemness in 3D Hydrogels Requires Matrix Remodelling," *Nature Materials* 16, no. 12 (2017): 1233–1242, https://doi.org/10.1038/nmat5020.

36. E. R. Komosa, W.-H. Lin, and B. M. Ogle, "Toward Robust and Reproducible Pluripotent Stem Cell Expansion in Bioprinted GelMA Constructs," *International Journal of Bioprinting* 11, no. 1 (2024): 363–381.

37. D. R. Griffin, W. M. Weaver, P. O. Scumpia, D. Di Carlo, and T. Segura, "Accelerated Wound Healing by Injectable Microporous Gel Scaffolds Assembled From Annealed Building Blocks," *Nature Materials* 14, no. 7 (2015): 737–744, https://doi.org/10.1038/nmat4294.

38. F. Jivan and D. L. Alge, "Bio-Orthogonal, Site-Selective Conjugation of Recombinant Proteins to Microporous Annealed Particle Hydrogels for Tissue Engineering," *Advanced Therapeutics* 3, no. 1 (2020): 1900148, https://doi.org/10.1002/adtp.201900148.

39. D. Rommel, M. Mork, S. Vedaraman, et al., "Functionalized Microgel Rods Interlinked Into Soft Macroporous Structures for 3D Cell Culture," *Advanced Science* 9, no. 10 (2022): 2103554.

40. A. C. Suturin, A. J. D. Krüger, K. Neidig, et al., "Annealing High Aspect Ratio Microgels Into Macroporous 3D Scaffolds Allows for Higher Porosities and Effective Cell Migration," *Advanced Healthcare Materials* 11, no. 24 (2022): 2200989, https://doi.org/10.1002/adhm.202200989.

41. S. Bulut, D. Günther, M. Bund, et al., "Cellular Architects at Work: Cells Building Their Own Microgel Houses," *Advanced Healthcare Materials* 13 (2024): 2302957.

42. J. Koh, D. R. Griffin, M. M. Archang, et al., "Enhanced In Vivo Delivery of Stem Cells Using Microporous Annealed Particle Scaffolds," *Small* 15, no. 39 (2019): 1903147.

43. B. N. Pfaff, C. C. Flanagan, and D. R. Griffin, "Microporous Annealed Particle (MAP) Scaffold Pore Size Influences Mesenchymal Stem Cell Metabolism and Proliferation Without Changing CD73, CD90, and CD105 Expression Over Two Weeks," *Advanced Biology* 8, no. 2 (2024): 2300482.

44. J. M. de Rutte, J. Koh, and D. Di Carlo, "Scalable High-Throughput Production of Modular Microgels for In Situ Assembly of Microporous Tissue Scaffolds," *Advanced Functional Materials* 29, no. 25 (2019): 1900071.

45. A. Ofner, D. G. Moore, P. A. Rühs, et al., "High-Throughput Step Emulsification for the Production of Functional Materials Using a Glass Microfluidic Device," *Macromolecular Chemistry and Physics* 218, no. 2 (2017): 1600472, https://doi.org/10.1002/macp.201600472.

46. T. E. Ludwig, M. E. Levenstein, J. M. Jones, et al., "Derivation of Human Embryonic Stem Cells in Defined Conditions," *Nature Biotechnology* 24, no. 2 (2006): 185–187, https://doi.org/10.1038/nbt1177.

47. R. Emig, C. M. Zgierski-Johnston, V. Timmermann, et al., "Passive Myocardial Mechanical Properties: Meaning, Measurement, Models," *Biophysical Reviews* 13, no. 5 (2021): 587–610, https://doi.org/10.1007/s12551-021-00838-1.

48. D. Gothard, S. J. Roberts, K. M. Shakesheff, and L. D. Buttery, "Controlled Embryoid Body Formation via Surface Modification and Avidin–Biotin Cross-Linking," *Cytotechnology* 61, no. 3 (2009): 135–144, https://doi.org/10.1007/s10616-010-9255-3.

49. Y. Kittel, L. P. B. Guerzoni, C. Itzin, et al., "Varying the Stiffness and Diffusivity of Rod-Shaped Microgels Independently Through Their Molecular Building Blocks," *Angewandte Chemie International Edition* 62, no. 44 (2023): 202309779, https://doi.org/10.1002/anie.202309779.

50. M. Schmidt, K. Zeevaert, M. H. Elsafi Mabrouk, R. Goetzke, and W. Wagner, "Epigenetic Biomarkers to Track Differentiation of Pluripotent Stem Cells," *Stem Cell Reports* 18, no. 1 (2023): 145–158, https://doi.org/10.1016/j.stemcr.2022.11.001.

51. G. E. Lyons, S. Schiaffino, D. Sassoon, P. Barton, and M. Buckingham, "Developmental Regulation of Myosin Gene Expression in Mouse Cardiac Muscle," *Journal of cell biology* 111 (1990): 2427–2436, https://doi.org/10.1083/jcb.111.6.2427.

52. C. Cao, L. Li, Q. Zhang, et al., "Nkx2.5: A Crucial Regulator of Cardiac Development, Regeneration and Diseases," *Frontiers in cardiovascular medicine* 10 (2023): 1270951, https://doi.org/10.3389/fcvm.2023.1270951.

53. P. A. W. Anderson, A. Greig, T. M. Mark, et al., "Molecular Basis of Human Cardiac Troponin T Isoforms Expressed in the Developing, Adult, and Failing Heart," *Circulation Research* 76, no. 4 (1995): 681–686, https://doi.org/10.1161/01.RES.76.4.681.

54. C. M. Snyder and N. S. Chandel, "Mitochondrial Regulation of Cell Survival and Death During Low-Oxygen Conditions," *Antioxidants & Redox Signaling* 11, no. 11 (2009): 2673–2683, https://doi.org/10.1089/ars.2009.2730.

55. L. M. Tiede, E. A. Cook, B. Morsey, and H. S. Fox, "Oxygen Matters: Tissue Culture Oxygen Levels Affect Mitochondrial Function and Structure as Well as Responses to HIV Viroproteins," *Cell Death & Disease* 2, no. 12 (2011): 246, https://doi.org/10.1038/cddis.2011.128.

56. A. Salas, A. Duarri, L. Fontrodona, et al., "Cell Therapy With hiPSC-Derived RPE Cells and RPCs Prevents Visual Function Loss in a Rat Model of Retinal Degeneration," *Molecular Therapy—Methods & Clinical Development* 20 (2021): 688–702, https://doi.org/10.1016/j.omtm.2021.02.006.

57. T. Akhtar, H. Xie, M. I. Khan, et al., "Accelerated Photoreceptor Differentiation of hiPSC-Derived Retinal Organoids by Contact Co-Culture With Retinal Pigment Epithelium," *Stem Cell Research* 39 (2019): 101491, https://doi.org/10.1016/j.scr.2019.101491.



15214095, 0, Downloaded from https://advanced.onlinelibrary.wiley.com/doi/10.1002/adma.75116, Wiley Online Library on [27/09/2026]. See the Terms and Conditions (https://onlinelibrary.wiley.com/terms-and-conditions) on Wiley Online Library for rules of use; OA articles are governed by the applicable Creative Commons License

58. J. Harkin, K. H. Peña, C. Gomes, et al., "A Highly Reproducible and Efficient Method for Retinal Organoid Differentiation From Human Pluripotent Stem Cells," *Proceedings of the National Academy of Sciences* 121, no. 25 (2024): 2317285121, https://doi.org/10.1073/pnas.2317285121.

59. X. Zhong, C. Gutierrez, T. Xue, et al., "Generation of Three-Dimensional Retinal Tissue With Functional Photoreceptors From Human iPSCs," *Nature Communications* 5, no. 1 (2014): 4047, https://doi.org/10.1038/ncomms5047.

60. D. Rommel, B. Häßel, P. Pietryszek, et al., "Thermally Assisted Microfluidics to Produce Chemically Equivalent Microgels With Tunable Network Morphologies," *Angewandte Chemie International Edition* 64, no. 1 (2025): 202411772, https://doi.org/10.1002/anie.202411772.

61. C. Licht, J. C. Rose, A. O. Anarkoli, et al., "Synthetic 3D PEG-Anisogel Tailored With Fibronectin Fragments Induce Aligned Nerve Extension," *Biomacromolecules* 20, no. 11 (2019): 4075–4087, https://doi.org/10.1021/acs.biomac.9b00891.

62. S. L. Zheng and K. M. Loh, "Creating Artificial Signaling Gradients to Spatially Pattern Engineered Tissues," *Current Opinion in Biotechnology* 78 (2022): 102810, https://doi.org/10.1016/j.copbio.2022.102810.

63. N. Gjorevski, M. Nikolaev, T. E. Brown, et al., "Tissue Geometry Drives Deterministic Organoid Patterning," *Science* 375, no. 6576 (2022): aaw9021, https://doi.org/10.1126/science.aaw9021.

64. Y. Xie, E.-S. Park, D. Xiang, and Z. Li, "Long-Term Organoid Culture Reveals Enrichment of Organoid-Forming Epithelial Cells in the Fimbrial Portion of Mouse Fallopian Tube," *Stem Cell Research* 32 (2018): 51–60, https://doi.org/10.1016/j.scr.2018.08.021.

65. S. L. Giandomenico, M. Sutcliffe, and M. A. Lancaster, "Generation and Long-Term Culture of Advanced Cerebral Organoids for Studying Later Stages of Neural Development," *Nature Protocols* 16, no. 2 (2021): 579–602, https://doi.org/10.1038/s41596-020-00433-w.

66. J. P. Licata, K. H. Schwab, Y.-E. Har-el, J. A. Gerstenhaber, and P. I. Lelkes, "Bioreactor Technologies for Enhanced Organoid Culture," *International Journal of Molecular Sciences* 24, no. 14 (2023): 11427, https://doi.org/10.3390/ijms241411427.

67. J. Lölsberg, J. Linkhorst, A. Cinar, A. Jans, A. J. C. Kuehne, and M. Wessling, "3D nanofabrication Inside Rapid Prototyped Microfluidic Channels Showcased by Wet-Spinning of Single Micrometre Fibres," *Lab on a Chip* 18, no. 9 (2018): 1341–1348, https://doi.org/10.1039/C7LC01366C.

68. D. Rommel, et al., "Functionalized Microgel Rods Interlinked Into Soft Macroporous Structures for 3D Cell Culture," *Advanced Science* 9, no. 10 (2022): 2103554.

69. S. Boesveld, Y. Kittel, Y. Luo, et al., "Microgels as Platforms for Antibody-Mediated Cytokine Scavenging," *Advanced Healthcare Materials* 12, no. 18 (2023): 2300695, https://doi.org/10.1002/adhm.202300695.

70. A. Kurtz, N. Mah, Y. Chen, et al., "Human Pluripotent Stem Cell Registry: Operations, Role and Current Directions," *Cell Proliferation* 55, no. 8 (2022): 13238, https://doi.org/10.1111/cpr.13238.

71. C. E. Strong, J. Zhang, M. Carrasco, et al., "Functional Brain Region-Specific Neural Spheroids for Modeling Neurological Diseases and Therapeutics Screening," *Communications Biology* 6, no. 1 (2023): 1211, https://doi.org/10.1038/s42003-023-05582-8.

72. Y. Yao, H. A. Coleman, L. Meagher, J. S. Forsythe, and H. C. Parkington, "3D Functional Neuronal Networks in Free-Standing Bioprinted Hydrogel Constructs," *Advanced Healthcare Materials* 12, no. 28 (2023): 2300801, https://doi.org/10.1002/adhm.202300801.

## Supporting Information

Additional supporting information can be found online in the Supporting Information section.

**Supporting File 1**: adma75116-sup-0001-SuppMat.docx.

**Supporting File 2**: adma75116-sup-0002-SuppMat.zip.



15214095, 0, Downloaded from https://advanced.onlinelibrary.wiley.com/doi/10.1002/adma.75116, Wiley Online Library on [27/09/2026]. See the Terms and Conditions (https://onlinelibrary.wiley.com/terms-and-conditions) on Wiley Online Library for rules of use; OA articles are governed by the applicable Creative Commons License